JOURNAL OF PETROLOGY

Journal of Petrology, 2020, Vol. 61, No. 9: egaa083
doi: 10.1093/petrology/egaa083
Advance Access Publication Date: 11 December 2020
Original Article

OXFORD

Fo and Ni Relations in Olivine Differentiate between Crystallization and Diffusion Trends

Boris Gordeychik [1,2,*], Tatiana Churikova[1,3], Thomas Shea[4], Andreas Kronz[1], Alexander Simakin[1,5] and Gerhard Wörner[1]

[1]Geowissenschaftliches Zentrum Göttingen, Abteilung Geochemie, Universität Göttingen, Göttingen 37077, Germany; [2]Institute of Experimental Mineralogy, Russian Academy of Sciences, Chernogolovka 142432, Russia; [3]Institute of Volcanology and Seismology, Far East Branch, Russian Academy of Sciences, Petropavlovsk-Kamchatsky 683006, Russia; [4]Department of Earth Sciences, University of Hawaii, Honolulu, HI 96822, USA; [5]Institute of Physics of the Earth, Russian Academy of Sciences, Moscow 123242, Russia

*Corresponding author. Telephone: +7(49652)25853. Fax: +7(49652)49687. E-mail: gordei@mail.ru

Received 19 August 2019; Accepted 15 August 2020

ABSTRACT

Nickel is a strongly compatible element in olivine, and thus fractional crystallization of olivine typically results in a concave-up trend on a Fo–Ni diagram. 'Ni-enriched' olivine compositions are considered those that fall above such a crystallization trend. To explain Ni-enriched olivine crystals, we develop a set of theoretical and computational models to describe how primitive olivine phenocrysts from a parent (high-Mg, high-Ni) basalt re-equilibrate with an evolved (low-Mg, low-Ni) melt through diffusion. These models describe the progressive loss of Fo and Ni in olivine cores during protracted diffusion for various crystal shapes and different relative diffusivities for Ni and Fe–Mg. In the case when the diffusivity of Ni is lower than that for Fe–Mg interdiffusion, then olivine phenocrysts affected by protracted diffusion form a concave-down trend that contrasts with the concave-up crystallization trend. Models for different simple geometries show that the concavity of the diffusion trend does not depend on the size of the crystals and only weakly depends on their shape. We also find that the effect of diffusion anisotropy on trend concavity is of the same magnitude as the effect of crystal shape. Thus, both diffusion anisotropy and crystal shape do not significantly change the concave-down diffusion trend. Three-dimensional numerical diffusion models using a range of more complex, realistic olivine morphologies with anisotropy corroborate this conclusion. Thus, the curvature of the concave-down diffusion trend is mainly determined by the ratio of Ni and Fe–Mg diffusion coefficients. The initial and final points of the diffusion trend are in turn determined by the compositional contrast between mafic and more evolved melts that have mixed to cause disequilibrium between olivine cores and surrounding melt. We present several examples of measurements on olivine from arc basalts from Kamchatka, and published olivine datasets from mafic magmas from non-subduction settings (lamproites and kimberlites) that are consistent with diffusion-controlled Fo–Ni behaviour. In each case the ratio of Ni and Fe–Mg diffusion coefficients is indicated to be <1. These examples show that crystallization and diffusion can be distinguished by concave-up and concave-down trends in Fo–Ni diagrams.

Key words: diffusion trend; fractional crystallization; Kamchatka; numerical diffusion modelling; olivine

INTRODUCTION

The compositions of basalts and their phenocrysts provide important constraints on the evolution of mantle-derived magmas and their ascent through the crust. Olivine is often one of the first major mineral phases to crystallize from primitive high-Mg and high-Ni basaltic melts and is stable across a large temperature range. The Mg and Ni contents of olivine

phenocrysts reflect this compositional change and can therefore provide important constraints on processes of their early history; that is, crystallization, mixing and assimilation, as well as conditions and duration of magma storage (e.g. Ariskin & Barmina, 2004; Costa & Chakraborty, 2004; Costa & Dungan, 2005; Costa *et al.*, 2008; Straub *et al.*, 2008, 2011; Wang & Gaetani, 2008; Costa & Morgan, 2010; Qian *et al.*, 2010; Kahl *et al.*, 2011, 2015; Ruprecht & Plank, 2013; Shea *et al.*, 2015*a*, 2015*b*; Bouvet de Maisonneuve *et al.*, 2016; Giuffrida & Viccaro, 2017; Lynn *et al.*, 2017*a*, 2017*b*, 2018; Matzen *et al.*, 2017; Oeser *et al.*, 2018; Ruth *et al.*, 2018; Gleeson & Gibson, 2019). Nonetheless, using the chemical composition and zoning of olivine crystals to reconstruct these processes is not straightforward. The observed compositional changes can be the result of both crystallization and/or diffusion, and unraveling their contribution to compositional zoning is required to extract meaningful interpretations. Additionally, the olivine cargo entrained to the surface is often heterogeneous in composition, partly because residence and diffusion times of individual crystals in a reservoir or mush system can vary significantly (e.g. Thomson & Maclennan, 2013). As a result, the cores of certain olivine crystals may be affected by diffusion of Fe–Mg and other fast-diffusing elements (such as Ni), whereas outer parts of the crystals record more recent processes such as crystallization.

Compositional variations between olivine crystals from a single sample, or within single crystals, are typically interpreted to result from fractional crystallization and/or magma mixing, and their study has become an important tool to better understand the pre-eruptive history of basaltic magmas (e.g. Costa & Dungan, 2005; Costa *et al.*, 2008; Straub *et al.*, 2008; Costa & Morgan, 2010; Qian *et al.*, 2010; Ruprecht & Plank, 2013; Kahl *et al.*, 2015). Element diffusion in crystals acts to homogenize zoning produced by disequilibrium between olivine and surrounding melt. Because different elements diffuse at specific rates, modelling diffusion allows estimation of the rates of various magmatic processes prior to eruption (Costa & Chakraborty, 2004; Costa & Dungan, 2005; Costa *et al.*, 2008; Costa & Morgan, 2010; Qian *et al.*, 2010; Kahl *et al.*, 2011, 2015; Ruprecht & Plank, 2013; Shea *et al.*, 2015*a*, 2015*b*; Bouvet de Maisonneuve *et al.*, 2016; Giuffrida & Viccaro, 2017; Lynn *et al.*, 2017*a*, 2017*b*, 2018; Gordeychik *et al.*, 2018; Oeser *et al.*, 2018; Ruth *et al.*, 2018; Albert *et al.*, 2020; Sundermeyer *et al.*, 2020).

Most approaches to modelling diffusion in olivine consider zoning at the outer crystal rim, assuming that concentration gradients represent the last stages of magma evolution (e.g. magma mixing) before eruption (e.g. Costa & Chakraborty, 2004; Costa & Dungan, 2005; Qian *et al.*, 2010; Lynn *et al.*, 2017*a*, 2017*b*; Sundermeyer *et al.*, 2020). Diffusion gradients that extend inside a crystal can be used to backtrack processes occurring over longer durations, such as magma transfer time from deeper crustal levels or even the mantle source (e.g. Ruprecht & Plank, 2013; Gordeychik *et al.*, 2018; Ruth *et al.*, 2018; Albert *et al.*, 2020). Although this is the best-suited approach to unravel the recent history of the crystals during a final magma mixing event and ascent, it may miss some valuable information contained in the inner cores of the crystals.

However, in some cases, initial core compositions can be completely lost for faster diffusing elements. If characterized and understood, core loss in different elements could therefore be leveraged to decipher the longer histories of magma transport and storage. In addition, identifying the compositional fingerprints of core homogenization may aid in understanding the underlying causes for the frequent chemical heterogeneity observed in erupted olivine populations. In the present study, we investigate the situation when diffusion time is long enough that Ni diffusion and Fe–Mg interdiffusion (hereafter referred to as Fo diffusion for simplicity) change the composition over the entire crystal, including the core. We analyse the effects of protracted diffusion on the Fo and Ni composition of olivine cores and show that these compositional variations can be distinguished from those associated with fractional crystallization. Our model shows that after protracted diffusion and loss of initial core compositions, olivine phenocrysts have higher Ni content (are 'Ni-enriched') at the same Fo in comparison with olivine phenocrysts that formed by fractional crystallization. Fo–Ni diagrams allow the processes of crystallization and diffusion to be distinguished, and can therefore be used to characterize natural Ni-enriched olivine compositions with different histories from a range of magmatic settings.

Natural examples of Ni-enriched olivine

'Ni-enriched' olivine crystals are abundant in mafic alkaline rocks such as lamproites (Prelević *et al.*, 2013) and kimberlites (Arndt *et al.*, 2006, 2010; Kamenetsky *et al.*, 2008, 2011; Cordier *et al.*, 2015; Sazonova *et al.*, 2015; Kargin *et al.*, 2017; Giuliani, 2018; Lim *et al.*, 2018; Mitchell *et al.*, 2019). The Fo–Ni diagram in Fig. 1a shows the gently sloping trend of olivine cores from a kimberlite sample, which is contrary to the steep crystallization trend recorded by the rims of olivine phenocrysts (Arndt *et al.*, 2006, 2010; Cordier *et al.*, 2015). Cordier *et al.* (2015) could successfully model only the trend of fractional crystallization recorded by the olivine rims (grey line in Fig. 1a). A similar observation was made for olivine crystals from a maar deposit at Shiveluch volcano (Fig. 1b). Our calculated crystallization trend in Fig. 1b starts at the highest Mg–Ni composition of the measured rims. As in Fig. 1a, we observe a second trend formed by the cores that is cross-cutting the fractional crystallization trend (albeit with fewer data points).

Thus, in both examples in Fig. 1 the fractional crystallization process describes well the rims of olivine crystals. However, the trend of olivine cores, including both high-Fo part and low-Fo part, is not explained. Several

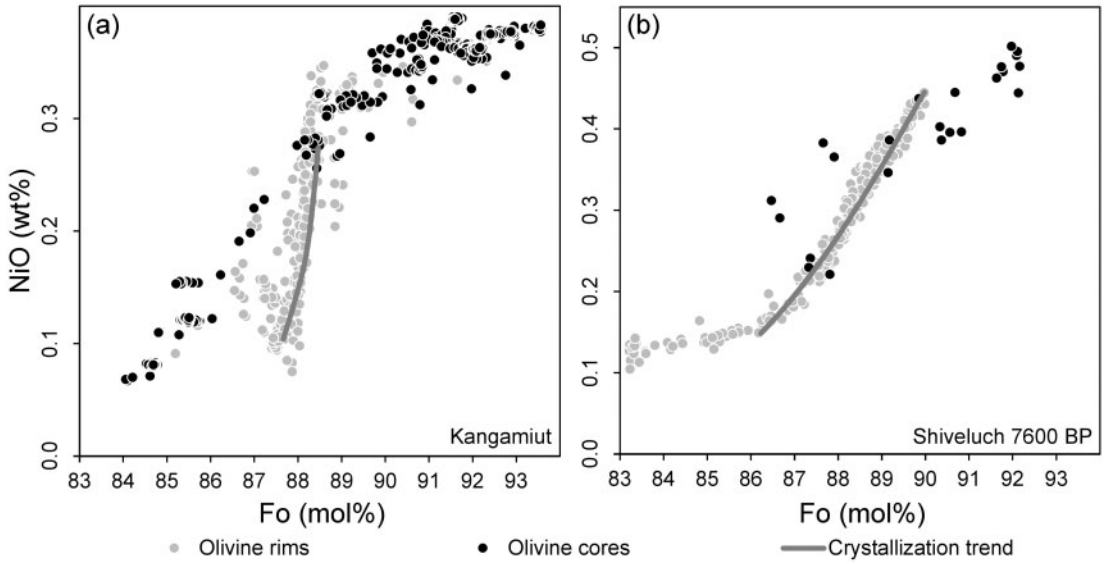

Fig. 1. Fo–Ni diagrams for olivine crystals from different natural environments. Black circles represent compositions of Ni-enriched olivine cores; grey circles show compositions of olivine rims, which record melt evolution at the final stage. (a) represents a well-documented example of a gently sloping trend formed by 'Ni-enriched' olivine cores from a kimberlite dyke from the Kangamiut region in West Greenland (Arndt *et al.*, 2006, 2010; Cordier *et al.*, 2015, 2016, 2017). The fractional crystallization trend calculated by Cordier *et al.* (2015) and shown by the grey line clearly crosscuts the gently sloping trend formed by the olivine cores. (b) Olivine phenocryst compositions from a basaltic andesite in a subduction setting, 7600 BP tuff ring on Shiveluch volcano, Kamchatka (Gordeychik *et al.*, 2018), showing a gentle trend of Ni-enriched cores that are overgrown by rims that follow a crystallization trend. This trend (grey line) was calculated with crystallization steps of 0·1%, Kd_{Mg} from Klöck & Palme (1988), Kd_{Fe}/Kd_{Mg} from Straub *et al.* (2008), and Kd_{Ni} from Hart & Davis (1978). The gentle trends of Ni-enriched core compositions as observed in (a) cannot form by fractional crystallization from a single parent magma. Outliers of Ni-rich cores that fall off to the right and left of the rim fractionation trend (b) also follow the same gentle trend.

researchers have attempted to model the gently sloping trend of olivine cores and the steep trend of rims by crystallization from the same high-Fo, high-Ni melt (fig. 4 of Cordier *et al.*, 2016; fig. 1 of Cordier *et al.*, 2017; Moore, 2017). These attempts were not successful because it would require unreasonable combinations of partitioning coefficients between Fe, Mg, and Ni in olivine and melt, which are not supported by experimental or natural partitioning data. Thus, at present, the trend formed by olivine rims is clearly described by the fractional crystallization process, whereas the gently sloping trend formed by olivine cores is not. Finding out the nature and properties of this trend is one of the main goals of the present research.

We refer to olivine core compositions that form the gentle sloping trend in Fo–Ni space as 'Ni-enriched'. The occurrence of the Ni-enriched olivine crystals falling off typical fractional crystallization trends (i.e. Fo–Ni decoupling in kimberlites) has been extensively debated (Cordier *et al.*, 2015, 2016, 2017; Giuliani & Foley, 2016; Moore, 2017). As our examples have shown (Fig. 1) Ni-enriched trends and trends following fractional crystallization can be observed in the same rock. However, the crystallization trend can also be completely absent (e.g. Sazonova *et al.*, 2015; Kargin *et al.*, 2017) and in those cases the Ni-enriched trend can be identified only because of its gentle slope that cannot be reproduced by crystallization processes.

Most studies attribute the unusual trend of Fo–Ni compositions from kimberlitic olivine to a compositionally diverse cargo of olivine grains from distinct and unrelated sources. Distinct Fo–Ni olivine compositions have thus been interpreted as mixtures of xenocrystic olivine crystals from metasomatized rocks (high-Fo and high-Ni part of the trend) and crystals that formed later from the host kimberlite melt (low-Fo, low-Ni olivine crystals) (Skinner & Clement, 1979; Skinner, 1986; Arndt *et al.*, 2006, 2010; Kamenetsky *et al.*, 2008; Giuliani & Foley, 2016; Kargin *et al.*, 2017; Moore, 2017; Lim *et al.*, 2018). Mitchell (1973, 1986) considered that inner cores consist of 40% of xenocrystic material and 60% crystallized from the host melt as rims of the crystals. Cordier *et al.* (2015) and Sazonova *et al.* (2015) also suggested a major role of metasomatic processes and explained the Fo–Ni decoupling as the result of interaction between mantle peridotites and kimberlite fluid or melt.

Other studies proposed that all or parts of olivine grains in kimberlites formed from the same melt by polybaric crystallization (Mitchell, 1973, 1986; Moore, 2017). Moore (2017) also suggested that decoupling of Fo and minor elements such as Ni and Ca is simply controlled by variable partition coefficients, because partition coefficients depend on P–T–fO_2–CO_2–H_2O or melt composition in different ways.

Most researchers, however, agreed that the gently sloping Fo–Ni trends observed in these studies are incompatible with simple fractional crystallization from the same melt (e.g. Kamenetsky *et al.*, 2008, 2011; Arndt *et al.*, 2010; Prelević *et al.*, 2013).

Straub *et al.* (2008) also convincingly showed that Ni-enriched olivine in intermediate (hybrid) lavas can be the result of olivine formation after magma mixing without the involvement of diffusion. In a new approach, Gleeson & Gibson (2019) combined magma mixing and diffusion. In both cases, steep crystallization trends shifted to the left were observed in Fo–Ni diagrams. Wang & Gaetani (2008) observed Fo–Ni trends in olivine from Hawaiian volcanoes that were clearly 'shallower' (i.e. little change in Ni vs Fo) than those associated with fractional crystallization. They tried to explain these trends qualitatively by repeated magma mixing and crystallization and came to the conclusion that such trends could be the result of equilibrium crystallization or re-equilibration of evolved basaltic melt and accumulated high-Fo/high-Ni olivine xenocrysts. Lynn *et al.* (2017*b*) and Gleeson & Gibson (2019) suggested that the primary controls on Ni contents in olivine from ocean island basalts are fractional crystallization, magma mixing, and diffusive re-equilibration.

Unusual olivine compositional trends with Ni-enriched olivine cores (Fig. 1b) were also recently found in subduction-related volcanic rocks from Kamchatka (Gordeychik *et al.*, 2018).

This brief review emphasizes that Ni-enriched olivine phenocrysts occur in different magmatic environments, that these compositions deviate clearly from the usual steep crystallization trend in the Fo–Ni diagram, and a multitude of different models have been put forward to explain these observations. In this study, we propose that Ni-enriched olivine cores form by diffusion after they are exposed to more evolved basaltic magmas after magma mixing. Diffusion models are developed to show that such Ni-enriched olivine crystals can be formed by protracted diffusion, and that the curvature of Fo–Ni trends reflects the ratio of Ni and Fo diffusion coefficients. We demonstrate that these relationships are robust and independent of olivine crystal sizes, shapes and anisotropy of diffusion, and for known thermodynamic and compositional conditions relevant to natural magmas, the ratio of Ni and Fo diffusion coefficients is always smaller than unity.

METHODS AND MODELS

Here, we examine the problem of loss of components by an olivine crystal owing to diffusion. We consider an initially homogeneous olivine crystal with a composition Fo_0 and Ni_0 formed in high-Mg and high-Ni silicate melt, being abruptly incorporated into a more evolved melt with lower Mg and Ni. We assume that the olivine density does not change significantly (Girona & Costa, 2013) and apply the diffusion equation (Crank, 1975):

$$\frac{\partial C}{\partial t} = \mathrm{div}\left(\boldsymbol{D}_C \cdot \mathbf{grad}(C)\right). \tag{1}$$

This equation is the conservation law of the diffusing component C in an anisotropic medium. The symbol C represents Ni component measured in wt%, or the Fo component $100Mg_\mu/(Mg_\mu + Fe_\mu)$ in mol%, respectively. Here the subscript μ means a component measured in moles. $\boldsymbol{D}_C$ is the diffusivity matrix $\boldsymbol{D}_{Fo}$ or $\boldsymbol{D}_{Ni}$ in the anisotropic olivine crystal. The diffusion process is controlled by the initial conditions, C_0 (Fo_0 or Ni_0) in the interior of the crystal, and by the boundary conditions, C_m (Fo_m or Ni_m) at the crystal margin in equilibrium with the surrounding more evolved melt (i.e. $Fo_0 > Fo_m$, $Ni_0 > Ni_m$). Where it is permissible for a simplification of the equations, we will use the non-dimensional concentration of the diffusing component Δ_C, so that the initial concentration in the center of the crystal will be $\Delta_C = 1$, and at the crystal margin it will be $\Delta_C = 0$.

$$\Delta_C = \frac{C - C_m}{C_0 - C_m}. \tag{2}$$

If the profile is parallel to the direction of the concentration gradient, and the concentration does not change in the directions perpendicular to the profile, then the diffusivity along the profile in the anisotropic media with principal crystallographic axes *a*, *b*, and *c* can be recovered using (Carslaw & Jaeger, 1959; Costa & Chakraborty, 2004; Chakraborty, 2010; Shea *et al.*, 2015*a*)

$$D_C^{pr} = D_C^a \cos^2\alpha + D_C^b \cos^2\beta + D_C^c \cos^2\gamma, \tag{3}$$

where D_C^a, D_C^b, and D_C^c are the diffusivities along *a*, *b*, and *c* and thus the diagonal elements of the matrix $\boldsymbol{D}_C$, and α, β, and γ are the angles between the profile direction and the principal axes. The anisotropic properties of Fo and Ni are similar, and the following relations are used (Costa & Chakraborty, 2004; Chakraborty, 2010):

$$D_C^a = D_C^b = D_C^c/6. \tag{4}$$

Because equations (3) and (4) are valid for Fo and Ni diffusion coefficients, their ratio is independent from profile direction $D_{Ni}^{pr}/D_{Fo}^{pr} = D_{Ni}^a/D_{Fo}^a = D_{Ni}^b/D_{Fo}^b = D_{Ni}^c/D_{Fo}^c$, and this ratio is a scalar quantity. Therefore, when considering the ratio of diffusion coefficients D_{Ni}/D_{Fo} below, we can omit the superscripts.

Next, we consider the problem of loss of elements by protracted diffusion out of an olivine core with a given initial composition, when the mathematical solution can no longer be considered as one-dimensional (1D). Similar issues were discussed briefly by Costa & Chakraborty (2004) and Shea *et al.* (2015*a*) for Fo diffusion, but not explored in the context of two elements with differing diffusivities. Also, Thomson & Maclennan (2013) suggested that diffusion affected the cores of crystals in a mush and developed simple models to describe the process. However, we will consider a more complex approach for the diffusion of two chemical components with different diffusivities (Fo and Ni). Therefore, the relationship between Fo and Ni as diffusing components is considered first.

Here, we use previously published data to test our theoretical considerations and models. We also present new measured data from natural examples of mafic arc

basalts of Kamchatka to support the model interpretations. Electron probe microanalysis (EPMA) of olivine phenocrysts was conducted with five wavelength-dispersive spectrometers using a JEOL JXA 8900RL instrument at the GZG (Geowissenschaftliches Zentrum Göttingen), Göttingen University. We used a specifically designed high-precision method based on increased current and increased voltage (Batanova *et al.*, 2015). The electron microprobe was configured at accelerating voltage of 20 kV, beam current of 300 nA, and a focused beam smaller than 5 μm in diameter. This configuration allowed us to analyse olivine profiles for major and trace elements with a spatial resolution up to 1 μm. Secondary electron imaging (SEI) were used to locate analytical profiles acquired within the analysed olivine phenocrysts. Backscatter electron images in compositional mode (COMPO) showed chemical zoning in olivine, where darker areas represent higher contents of the light element Mg and bright areas correspond to relatively higher content of Fe. The orientation of the measured profile relative to the crystallographic axes of the crystals was determined using a scanning electron microscope (SEM) Quanta 200 F with an electron backscatter detector (EBSD) at the GZG. Further details of methods used, including standards and references, are given in Supplementary Data Tables 1.1 and 1.2 of Gordeychik *et al.* (2018); supplementary data are available for downloading at http://www.petrology.oxfordjournals.org.

Relative diffusivities of Fo and Ni

Owing to the large number of experimental studies, the diffusion coefficients for Fo and Ni in olivine are available for olivine with various Fo content, for temperatures of 750–1400 °C, from 1 bar to 120 kbar pressure, and for oxygen fugacities between 10^{-10} and 10^{-4} Pa (see review by Chakraborty, 2010). Dohmen & Chakraborty (2007) and Chakraborty (2010) built a set of formulae that quantitatively describe the dependences of Fo and Ni diffusivities on olivine Fo, P–T–fO_2 conditions, and crystal orientation. The formulae were constructed on the basis of the results of several experimental studies by Dohmen *et al.* (2007) for Fo and Petry *et al.* (2004) and Holzapfel *et al.* (2007) for Ni diffusion coefficients. Despite the significant scatter in experimental results, it was noted that the Ni diffusion coefficient may be slightly lower compared with Fo (Dohmen *et al.*, 2007; Chakraborty 2010). In contrast, based on natural olivine compositions, other researchers suggested that Ni might diffuse slightly faster than Fo under some conditions (e.g. table 7.1 of Costa & Morgan, 2010; fig. 1 of Lynn *et al.*, 2018). Given these uncertainties, we first evaluate the existing information about the relative diffusivities of Fo and Ni, which is crucial for the analysis of Fo–Ni relationships.

In principle, if zoning in a natural olivine crystal can be attributed to diffusion and not growth (e.g. Costa *et al.*, 2008; Kahl *et al.*, 2011; Shea *et al.*, 2015*b*), then Fo and Ni variations can be used to assess the relative values of their diffusivities. Compositional changes inside a crystal immersed in an evolved melt can be described using the analytical 1D solution of the diffusion equation with constant coefficients in a semi-infinite media (equation 3.13 of Crank, 1975), which is a commonly used approach (e.g. Holzapfel *et al.*, 2007; Costa *et al.*, 2008; Qian *et al.*, 2010; Costa & Morgan, 2010):

$$\Delta_C = \mathrm{erf}\left(\frac{x - x_b}{\delta_C}\right), \tag{5}$$

where erf is the error function, x is the coordinate along the profile perpendicular to the crystal surface and x_b is the position of the crystal margin. The characteristic width of the diffusion zone δ_C for the C component is given by the expression

$$\delta_C = 2\sqrt{D_C^{pr} t}, \tag{6}$$

where the scalar value D_C^{pr} is the diffusion coefficient along the profile [equation (3)] and t is time. Equation (6) shows that the characteristic width δ_C of the diffusion zone (hereafter simply referred to as 'width' for brevity) increases proportionally to the square root of the diffusion coefficient (see also Costa *et al.*, 2008). Hence, time can be cancelled out from equation (6) for Fo and Ni, and the ratio of the D_{Ni}/D_{Fo} coefficients can be written

$$\frac{D_{Ni}}{D_{Fo}} = \left(\frac{\delta_{Ni}}{\delta_{Fo}}\right)^2. \tag{7}$$

Combined measurements of Fo and Ni in zoned olivine phenocrysts have been documented in several studies (Costa & Dungan, 2005; Qian *et al.*, 2010; Ruprecht & Plank, 2013; Bouvet de Maisonneuve *et al.*, 2016; Lynn *et al.*, 2017*a*, 2017*b*, 2018; Gordeychik *et al.*, 2018; Ruth *et al.*, 2018; Albert *et al.*, 2020; Sundermeyer *et al.*, 2020). The data from some of these studies make it possible to evaluate the ratios of diffusion coefficients by two approaches: through the widths of diffusion zones using equation (7) and using formulae after Chakraborty (2010).

Estimates of Fo and Ni diffusivities through diffusion zone widths

Olivine compositions measured along some profiles with distinct Fo and Ni diffusion zones (Costa & Dungan, 2005; Qian *et al.*, 2010; Lynn *et al.*, 2017*a*, 2017*b*, 2018) were used to determine the coefficients in equation (5) by the least-squares method. Thus, the parameters of the analytical solution [equation (5)] were determined separately for Fo and for Ni for each profile considered, namely, the initial conditions Fo_0 and Ni_0 inside a crystal, the boundary conditions Fo_m and Ni_m at the crystal margin, and δ_{Fo} and δ_{Ni}—the diffusion zone widths for Fo and Ni, respectively. The coordinate x_b represents the crystal boundary. The ratios of Ni and Fo diffusion coefficients extracted from the ratios of

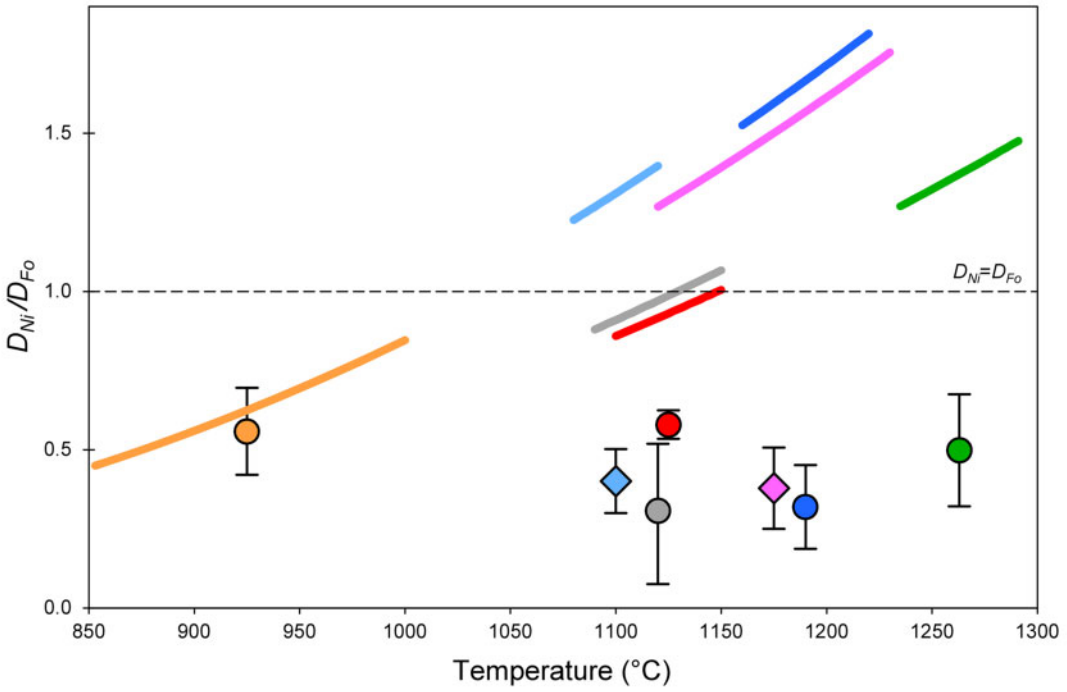

Volcano studied	D_{Ni}/D_{Fo} through δ_{Ni}/δ_{Fo}	Number of used profiles	Compositional and thermodynamic conditions				D_{Ni}/D_{Fo} after (Chakraborty, 2010)
			Fo (mol%)	Temperature interval (°C)	Pressure (bar)	Fugacity buffer	
Tatara-San Pedro (Costa & Dungan, 2005)		2	82	1100-1150	3000	NNO	
Handan-Xingtai (Qian *et al*., 2010)		4	91	850-1000	4000	QFM+0.75	
Kīlauea (Lynn *et al*., 2017a, b, 2018)		5	85	1235-1291	850	QFM	
Shiveluch 7600 BP (Gordeychik *et al*., 2018)		8	90	1160-1220	8000	QFM+1	
Paricutin 1943-1952 AD (Albert *et al*., 2020)		5	82	1090-1150	3000	QFM+1	
Shiveluch 3600 BP (this study)		3	86	1080-1020	8000	QFM+2.1	
Klyuchevskoy, high-Mg basalt (this study)		2	87	1120-1230	7500	QFM+1.3	

Fig. 2. Relative values of diffusion coefficients for Fo and Ni in olivine expressed as D_{Ni}/D_{Fo} for different natural examples. Each symbol represents an average value of D_{Ni}/D_{Fo} ratio calculated by equation (7) for several profiles from natural examples found in the literature. The error bars reflect the average of the absolute deviations for several profiles considered from each example; the number of profiles can be seen in the legend. All results show the diffusion coefficient ratio D_{Ni}/D_{Fo} to be less than unity. Colored curves show the D_{Ni}/D_{Fo} ratio calculated by formulae from Chakraborty (2010) for the corresponding compositional and thermodynamic conditions in the legend. The length of each color curve along the horizontal axis reflects the temperature interval from the corresponding publication. The temperatures and other thermodynamic conditions for the products of the 3600 BP Shiveluch eruption were based on Gorbach & Portnyagin (2011) and Nekrylov *et al.* (2018), and those for lavas from the Bulochka and Novograblenov cones on Klyuchevskoy volcano were based on Mironov & Portnyagin (2011), Mironov *et al.* (2015) and Nekrylov *et al.* (2018). Fugacity was calculated following the formulae from Ballhaus *et al.* (1991). Calculated by formulae from Chakraborty (2010), D_{Ni}/D_{Fo} ratios dramatically increase and become greater than unity above a temperature of 1000–1100 °C (see text for discussion).

diffusion zone widths using equation (7) for several natural examples (Costa & Dungan, 2005; Qian *et al.*, 2010; Lynn *et al.*, 2017*a*, 2017*b*, 2018; Albert *et al.*, 2020) show that the diffusion coefficient ratio D_{Ni}/D_{Fo} is always less than unity (Fig. 2).

The zoning patterns studied previously were generally measured near the olivine margins. However, a range of edge phenomena (e.g. quenching or crystal growth during fractional crystallization) can influence the zoning patterns in olivine rims. Therefore, better information should be gained from diffusion zones inside crystals for comparison of different element diffusivities. For example, Ruprecht & Plank (2013) studied internal diffusion zones where steeper Ni gradients persist whereas Fo gradients flatten out, or even Fo is entirely homogenized in the interior of olivine phenocrysts, which again argues for D_{Ni}/D_{Fo} ratios smaller than unity.

Complexly zoned olivine phenocrysts from the 7600 BP Shiveluch eruption preserve distinct Fo and Ni concentration gradients at the transition zone between low-Fo low-Ni cores and high-Fo high-Ni overgrowths (Fig. 3a). The transition zones between cores and overgrowths are always narrower for Ni than for Fo. Other elements with even lower diffusivities, such as chromium, aluminium and phosphorus, are still narrower. The boundary between core and overgrowth is marked

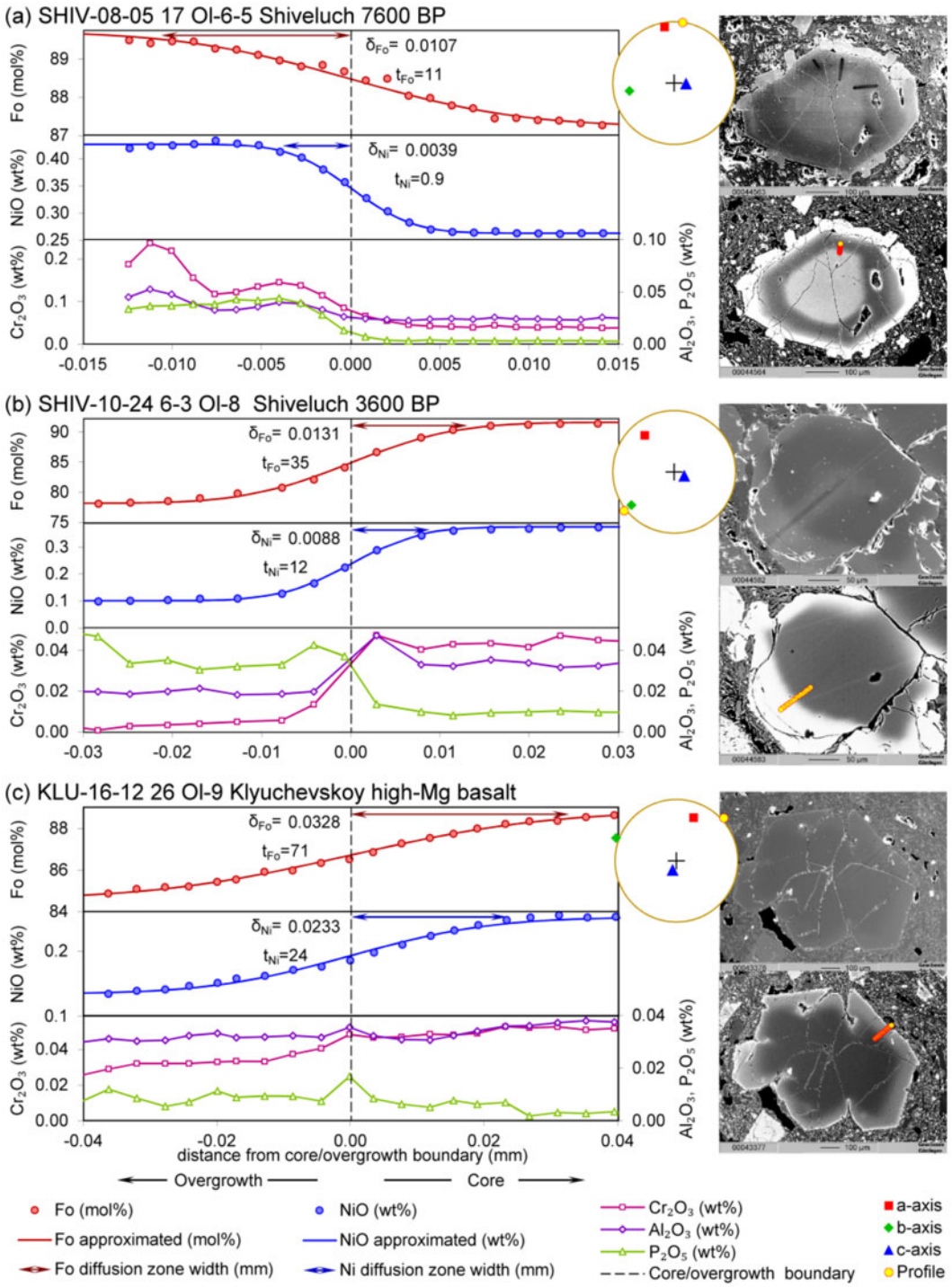

Fig. 3. Comparison of the diffusion zone widths for Fo and Ni in representative core–overgrowth profiles inside the olivine phenocrysts from several Kamchatka rocks: (a) 7600 BP Shiveluch eruption; (b) 3600 BP Shiveluch eruption; (c) Bulochka and Novograblenov monogenetic cones on the slope of Klyuchevskoy volcano. The zero point on the *x*-axis and dashed line represent the boundary between core (right) and overgrowth (left) as determined by the steepest compositional gradients. The projections of crystallographic axes *a*, *b*, and *c* of the crystal as well as EPMA profile orientation are shown in a stereographic lower hemisphere plot. The secondary electron image shows the olivine phenocryst in thin section with the trace of measured profiles indicated. The backscatter electron image in compositional mode (COMPO), which demonstrates the difference in atomic number over a sample, shows the transition zone between core and overgrowth as a gradient in grey scale and shows the position of the measured profile. The continuous blue and red lines show the analytical solutions for diffusion in a semi-infinite media [equation (5)] for Ni and Fo, respectively. Arrows with values mark the Fo and Ni diffusion zone widths, which were used to calculate relative diffusivities as $D_{Ni}/D_{Fo} = 0{\cdot}16$ for (a), 0·45 for (b), and 0·51 for (c) using equation (7). Cr–Al–P plot shows variations in olivine composition across the core–overgrowth boundary. All measured data for (a) have been given by Gordeychik *et al.* (2018), and those for (b) and (c) are given in the Supplementary Data Tables SM-1 and SM-2.

by the inflection point with the steepest gradient, and coincides for all measured elements. A simple diffusion model of a semi-infinite space (Crank, 1975) can be used to describe symmetrical Fo and Ni profiles across the core–overgrowth boundary with coordinate x_b [equation (5)]. The widths of the diffusion zones δ_{Fo} and δ_{Ni} are then determined by approximating the analytical solution given in equation (5) using a least-squares method. The ratio of these widths δ_{Ni}/δ_{Fo} is about 0·4 (Fig. 3a). For other profiles in olivine phenocrysts from the 7600 BP Shiveluch eruption, Gordeychik *et al.* (2018) determined the δ_{Ni}/δ_{Fo} ratio as 0·4–0·6 or D_{Ni}/D_{Fo} of $0{\cdot}3 \pm 0{\cdot}1$ (Fig. 2).

Newly collected Fo and Ni data on olivine crystals from lavas and tephra of the 3600 BP Shiveluch eruption (Fig. 3b) and from lavas of the Bulochka and Novograblenov cones on the NE slope of Klyuchevskoy volcano (Fig. 3c) give similar Fo–Ni diffusion relationships (Supplementary Data Tables SM-1 and SM-2). Despite their different origin, these olivine phenocrysts systematically show that the core–overgrowth transition zone is narrower in Ni compared with Fo (Fig. 3b and c) with calculated diffusivity ratios of $D_{Ni}/D_{Fo} = 0{\cdot}45$ for the 3600 BP Shiveluch eruption and $D_{Ni}/D_{Fo} = 0{\cdot}51$ for Klyuchevskoy basalts (Fig. 2).

Calculation of Fo and Ni diffusivities from existing formulae

The colored curves in Fig. 2 show D_{Ni}/D_{Fo} ratios as a function of temperature calculated from formulae (Chakraborty, 2010, pp. 617 and 618). The ratios of diffusion coefficients obtained through these expressions are in good agreement with the ratios obtained from Fo and Ni widths in natural olivine at temperatures of 850–1000 °C. However, at temperatures above 1100 °C, D_{Ni}/D_{Fo} ratios calculated after Chakraborty (2010) exceed unity and thus overestimate width-derived ratios by up to a factor of five (see Fig. 2).

Estimates of diffusion times in natural olivine through Fo and Ni

For every Fo and Ni profile shown in Fig. 3, the diffusion time, i.e. the time elapsed between the formation of overgrowth and the eruption of the lava and its phenocrysts, can be determined by the diffusion zone width and the diffusion coefficient through equation (6). If the ratio D_{Ni}/D_{Fo} is correct, Fo and Ni profiles in the same olivine should yield the same diffusions time (e.g. Costa & Dungan, 2005).

To test this, calculations for each crystal were carried out with appropriate thermodynamic conditions (see the legend in Fig. 2), and taking into account the orientation of the crystallographic axes (Fig. 3 and Supplementary Data Table SM-2). The Fo profiles give diffusion times t_{Fo} of 11, 35, and 71 days for the 7600 BP Shiveluch eruption, the 3600 BP Shiveluch eruption and high-Mg basalts of Klyuchevskoy, respectively. By contrast, diffusion times determined from Ni profiles t_{Ni} are 0·9, 12, and 24 days, respectively (Fig. 3). Thus, we have factor of 3–12 difference between Fo and Ni timescales. Similar factors of 2–16 were found for Fo and Ni diffusion times in zoned olivine phenocrysts of Paricutin volcano (supplementary data fig. S6 of Albert *et al.*, 2020). Such a difference leads us to conclude that calculations for Fo and Ni diffusion coefficients based on formulae from Chakraborty (2010) may not be applicable in all cases and these formulae should be used with some caution.

The discrepancies in timescale estimates obtained through Fo and Ni and in their diffusivities ratios are systematic in all the natural examples considered. It appears that the D_{Ni}/D_{Fo} relationship may be poorly constrained by experimental calibrations as stated by Holzapfel *et al.* (2007): 'Fo and Ni diffusion coefficients are similar within experimental uncertainties'. Our natural samples suggest instead that the diffusivity ratio is always lower than unity. This inconsistency may be due to differing P–T–fO_2 conditions between experimental studies and these natural olivine crystals, as suggested by Oeser *et al.* (2018) in the case of chromium. It is also possible that the compositional and/or thermodynamic conditions for the natural samples under consideration are outside the permissible limits of the validity of the applied formulae (Chakraborty, 2010). Based on our survey of natural examples, and as a basis for further discussion here, we argue that for a range of pressures, temperatures, and oxygen fugacity applicable to a range of natural magmas containing high-magnesium olivine, the diffusion coefficient of Ni should always be lower than that of Fo.

The Kamchatka rocks studied here were formed at temperatures above 1000 °C (Fig. 2), and Fo–Ni diffusion ratios for these rocks calculated through formulae from Chakraborty (2010) do not satisfy the condition $D_{Ni}/D_{Fo} < 1$. Therefore we cannot conduct our analysis further using these formulae. Instead we assume that Fo and Ni changes and their effect on diffusion coefficients are not too large and that D_{Ni}/D_{Fo} is indeed always <1. These assumptions allow us to construct dimensionless theoretical models for describing Fo–Ni distributions of olivine crystals undergoing protracted diffusion. Our obtained model results can then be compared with observed Fo–Ni distributions of olivine crystals in the studied rocks.

The analogy between diffusion and heat conductivity

As noted by Bird *et al.* (2002), 'A large number of diffusion problems can be solved by simply looking up the solutions to the analogous problems in heat conduction. When the differential equations and the boundary and initial conditions for the diffusion process are of exactly the same form as those for the heat conduction process, then the heat conduction solution may be taken over with appropriate changes in notation.' The diffusive exchange of elements between olivine and surrounding melt is similar to the problem of cooling a body immersed in a medium with a constant

temperature. Both problems are described by the same equations and boundary conditions, which differ in notation only. The constant boundary condition C_m at the crystal margin corresponds to a large Biot number in heat transfer problems, when the temperature at the surface of the body and the surrounding environment is constant. A constant melt composition may be attained if the processes of diffusion, mixing, and convection in the liquid are sufficiently rapid that the liquid remains homogeneous at the timescales considered.

Newton (1701) discovered the exponential decrease of temperature of a heated body with time *t*, and Newton's law of cooling for our compositional notation can be written as

$$\Delta_C = e^{-\frac{t}{\tau_C}}, \tag{8}$$

where τ_C is the relaxation time; for the case of diffusion it can be called the homogenization time (Besson, 2011). If Fo or Ni in an olivine phenocryst is not in equilibrium with surrounding melt, then non-dimensional concentration of these components will decrease with time τ_{Fo} (τ_{Ni}) by e times, where e is the base of the natural logarithm. The homogenization times τ_{Fo} and τ_{Ni} depend on crystal size, crystal shape, and diffusion coefficients. It should be noted that Newton's law is asymptotic; that is, it does not consider both the internal structure of the object and the initial stage of the process.

Fo–Ni diffusion trends in olivine

Under simultaneous Fo and Ni diffusion in an olivine crystal, time can be cancelled out and equation (8) can be reduced to a formula where Ni is a function of Fo:

$$\Delta_{Ni} = (\Delta_{Fo})^{\frac{\tau_{Fo}}{\tau_{Ni}}}. \tag{9}$$

The Ni vs Fo power function establishes a relationship between the losses of chemical components by the crystal during diffusion. It should be noted that the size, morphology, and anisotropic properties of the crystal have no explicit effect on the shape of the power function obtained through the adaptation of Newton's cooling law to the diffusion problem. The shape of the power function is determined by the relation between the homogenization times, which in turn are determined by Fo–Ni diffusion coefficients. We show above that the diffusion coefficient for Ni is lower than that for Fo in natural olivine phenocrysts. This means that Ni loss is slower than Fo loss, and Ni homogenization time should be longer than Fo homogenization time. Thus, the homogenization time ratio is smaller than unity and equation (9) is a concave-down function (Fig. 4a).

Similarly to Newton's law, which does not consider the internal structure of the cooling body, equation (9) does not consider the spatial distributions of the Fo–Ni diffusion coefficients inside the crystal; those distributions can only affect the values of the homogenization times. To study the Fo–Ni relation during diffusion [equation (9)], we assume that the diffusion coefficients inside the crystal do not change significantly. Then the connection between homogenization times and diffusion coefficients can be identified from similitude theory using the π-theorem (Kline, 1986):

$$\frac{\tau_{Fo}}{\tau_{Ni}} = \frac{D_{Ni}}{D_{Fo}}, \tag{10}$$

and it is possible to rewrite equation (9) in the form

$$\Delta_{Ni} = (\Delta_{Fo})^{\frac{D_{Ni}}{D_{Fo}}}. \tag{11}$$

This power function is plotted for different D_{Ni}/D_{Fo} ratios from 0·1 to 1 in Fig. 4a. This range in D_{Ni}/D_{Fo} covers the complete range of relative diffusion coefficients documented by Chakraborty (2010) at $Fo_{70–90}$ for temperatures from 750 to 1000 °C, $P = 10^5$–10^9 Pa, and for fO_2 of the quartz–fayalite–magnetite (QFM) — nickel–nickel oxide (NNO) buffer.

All crystals experiencing diffusion and having the same ratio of diffusion coefficients will move along the same path in the Fo–Ni diagram (Fig. 4a). The curvature of these paths depends on D_{Ni}/D_{Fo} only. Below we will consider these paths as diffusion trends with respect to natural samples. The curvature of such diffusion trends has a simple physical significance: if D_{Ni}/D_{Fo} is <1, which, as we argue above should be applicable to most natural olivine phenocrysts, then Ni losses from the crystal are slower than Fo losses and the crystal will be lowered in Fo faster than it is lowered in Ni. As a result, the smaller Ni diffusion coefficient is compared with Fo diffusion coefficient, the more the Fo depletion of the crystal is pronounced, thus increasing the downward concavity of the diffusion trend (Fig. 4a).

The concave-down curvature of olivine diffusion trends in the Fo–Ni diagram is distinctly different from Fo–Ni relations in olivine resulting from crystallization. Because Ni is a compatible element, olivine phenocrysts formed during crystallization produce a concave-up trend in Fo–Ni diagrams (e.g. Ariskin & Barmina, 2004; Costa *et al.*, 2008; Straub *et al.*, 2008, 2011; Wang & Gaetani, 2008; Ruprecht & Plank, 2013; Nishizawa *et al.*, 2017). A large number of examples with concave-up crystallization trends are shown in the paper by Matzen *et al.* (2017). Therefore, the contrast between the concave-down diffusion trend and concave-up crystallization trend is critical in distinguishing between these two processes, and we will present and discuss various natural examples of such contrasting trends below.

The influence of crystal shape and size on diffusion behaviour

The diffusion analogue [equations (9) and (11)] of Newton's cooling law [equation (8)] does not take into account the anisotropic properties of the crystal, nor its shape or size. The influence of these factors on the Ni vs Fo diffusion trend, if any, should be strongest during

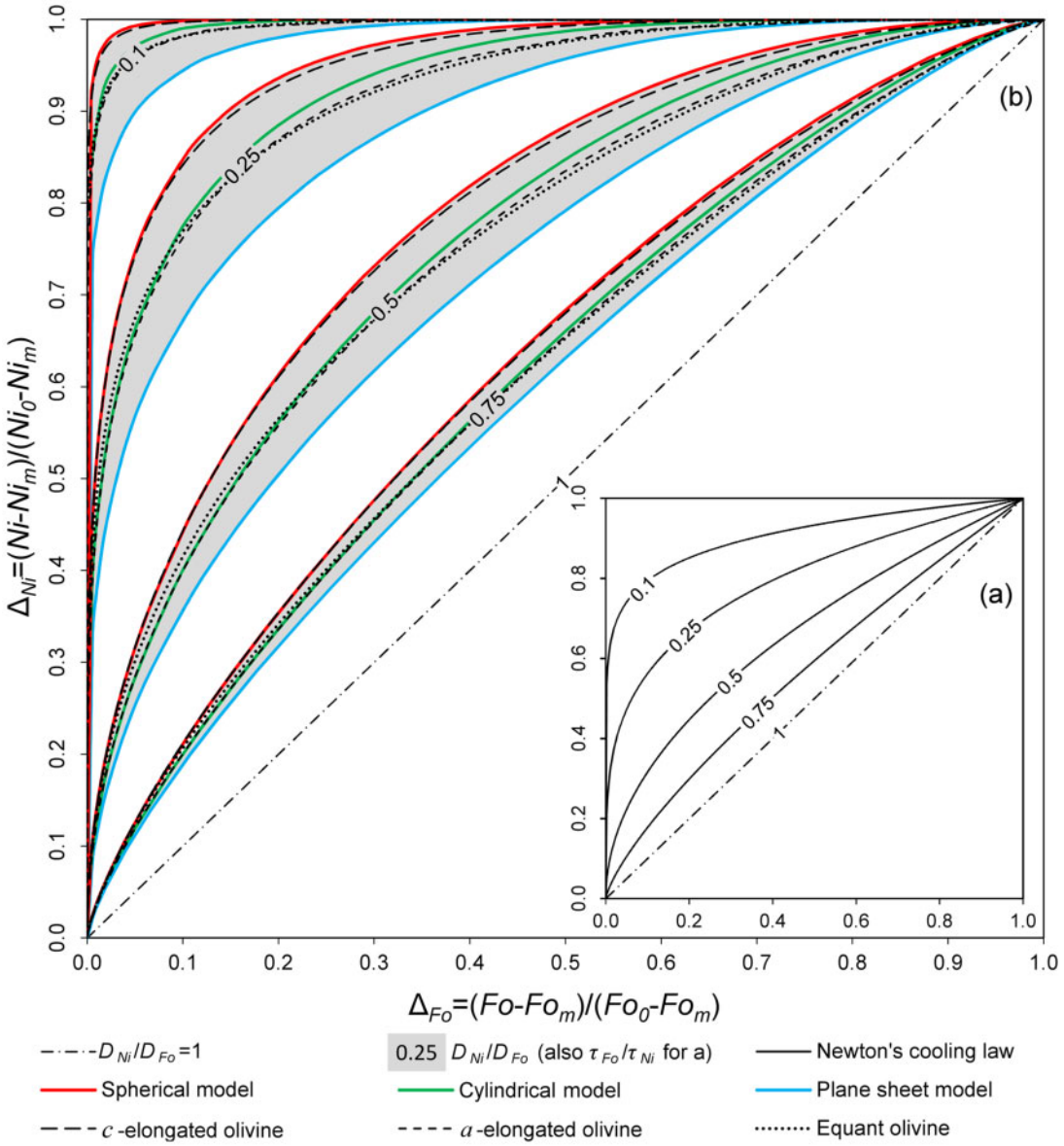

Fig. 4. Diffusion trends in non-dimensional coordinates Δ_{Fo} and Δ_{Ni} [equation (2)]. (a) Diffusion trends are as derived from Newton's cooling law for different τ_{Fo}/τ_{Ni} ratios [equation (9)] or for different D_{Ni}/D_{Fo} ratios [equation (11)]; these ratios are labelled on the curves. (b) Diffusion trends calculated for analytical models for the different geometries and for 3D calculations of diffusion in olivine phenocrysts with realistic shapes. Red lines are diffusion trends for the spherical model; green lines are for the cylindrical model; blue lines are for the plane sheet model. Grey shaded fields are regions of diffusion trends for a particular diffusion coefficient ratio for different sizes and shapes of olivine crystals. Dashed lines show diffusion trends defined by the 3D diffusion calculations for olivine crystals: the long dashed lines represent curved diffusion trends within *c*-elongated olivine crystals, medium-dashed lines represent diffusion trends of *a*-elongated olivine, and the short-dashed lines are the diffusion trends of the equant-shaped olivine.

the initial time when the behaviour of the solution has not yet reached the asymptotic stage.

The shape of natural olivine grains is variable and exhibits a number of different habits that can be related to undercooling and/or cooling rate during crystallization (Donaldson 1976; Deer *et al.*, 2013). To determine the effect of crystal shape on the position and curvature of the diffusion trend, we consider several models for possible end-member habits: isometric, columnar, and tabular. Because the aim of this section is to find the effect of crystal habits on the diffusion trend, all models are constructed for isotropic diffusion with coefficient D_C; the influence of anisotropy will be considered in the next section.

For the isometric crystal, a simple sphere is chosen as model with radius R and uniform initial distributions of components C_0. The sphere is put in contact with the melt at equilibrium with a composition C_m. The solution to compute the element concentration at the centre of the sphere is given by equation 6.19 of Crank (1975):

$$\Delta_C = 2\sum_{n=1}^{\infty}(-1)^{(n+1)}\exp\left(-\pi^2 n^2 \frac{D_C t}{R^2}\right). \quad (12)$$

There is a simple connection between equation (12) and Newton's cooling law [equation (8)]: Newton's cooling law is the first member of the sum in equation (12), with time shifted by some constant. This means that Newton's cooling law and equation (12) are asymptotically close each other (Fig. 5). This observation allows us to obtain an expression for the homogenization time of Fo discussed above:

$$\tau_C = \frac{R^2}{\pi^2 D_C}. \quad (13)$$

Then, using the characteristic crystal size d instead of the sphere diameter and the characteristic diffusion coefficient of Fo along the *a*- or *b*-axis [equation (4)] instead of D_C, we obtain for the homogenization time of Fo:

$$\tau_{Fo} = \frac{3d^2}{2\pi^2 \tilde{D}^c_{Fo}}, \quad (14)$$

where d is the characteristic crystal size and $\tilde{D}^c_{Fo}$ is the characteristic diffusion coefficient of Fo along the *c*-axis.

A circular cylinder is chosen to simulate an elongate (columnar) crystal. We consider a 1D axisymmetric cylinder of radius R with uniform initial distributions of component C_0. In this case, the solution for concentration along the axis of the cylinder is expressed as (equation 5.22 of Crank, 1975)

$$\Delta_C = \sum_{n=1}^{\infty}\frac{2}{\varepsilon_n J_1(\varepsilon_n)}\exp\left(-\varepsilon_n^2 \frac{D_C t}{R^2}\right), \quad (15)$$

where ε_n are the positive roots of the equation $J_0(\varepsilon_n) = 0$; J_0 and J_1 are the Bessel functions of the first kind of order zero and unity. The solution for the cylindrical model has a flatter appearance compared with the spherical model and is shown by a green line in Fig. 5.

A plane sheet geometry is considered as the end-member for a tabular crystal. We consider a plane sheet with thickness $2R$, with uniform initial distributions of the components C_0 that has a solution (equation 4.17 of Crank, 1975)

$$\Delta_C = \frac{4}{\pi}\sum_{n=0}^{\infty}\frac{(-1)^n}{2n+1}\exp\left[-\frac{\pi^2(2n+1)^2}{4}\cdot\frac{D_C t}{R^2}\right]. \quad (16)$$

The solution for the plane sheet model has a flatter appearance compared with both previous models and is indicated by a blue line in Fig. 5.

Each solution expressed by equations (12), (15), and (16) contains a series of exponents that do not allow a simple analytical reduction to the dependences Ni = Ni(Fo), as in the case of Newton's cooling law. Therefore, to construct Fo–Ni diagrams for different crystal habits, the parametric representation of Fo and Ni through dimensionless time t_{Fo} was used:

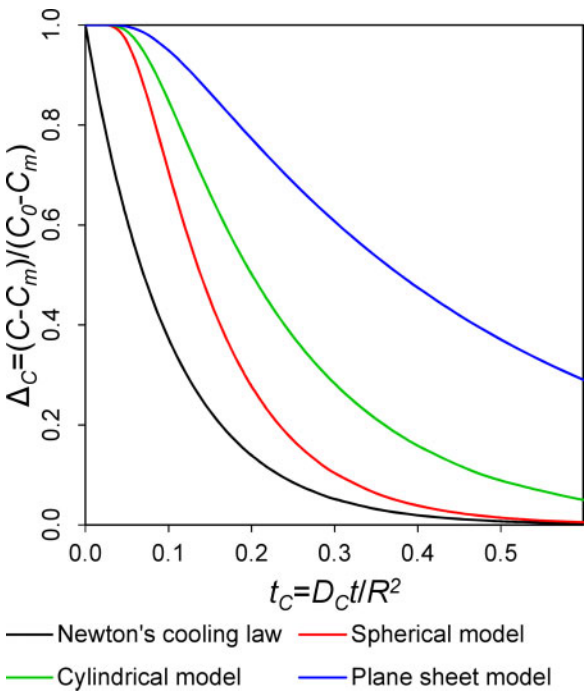

Fig. 5. Decreasing concentrations of a diffusing component C (Fo or Ni) calculated by different analytical models versus non-dimensional time t_C. Black line shows Newton's cooling law [equation (8)]. The colored lines show decreasing concentrations in the centres of crystals with different habits: spherical model for isometric crystal [equation (12)], cylindrical model for columnar crystal [equation (15)], and plane sheet model for a tabular crystal [equation (16)]. Newton's law shows a simple exponential decrease, as asymptotic law. By contrast, the models for different habits show an initial stage of diffusion with slowly decreasing values, after which the transition to an exponential decrease occurs.

$$t_{Fo} = \frac{D_{Fo} t}{R^2}, \quad (17)$$

$$\Delta_{Fo} = S(t_{Fo}), \quad (18)$$

$$\Delta_{Ni} = S(t_{Ni}) = S\left(\frac{D_{Ni}}{D_{Fo}} t_{Fo}\right), \quad (19)$$

where for Fo or Ni, as a solution S, one of the equations (12), (15), and (16) is implied, depending on the considered model. The parametric representation [equations (18) and (19)] shows that the characteristic dimension of each model considered (i.e. the radius of a sphere or a cylinder, or the half thickness for a plane sheet) plays no role in the calculated diffusion trend. That is, all crystals within the same model, regardless of their size, will move along the same trend. Only a change in the ratio of the diffusion coefficients can therefore influence the shape of the diffusion trend.

In detail, significant differences between the solutions for the different crystal habits can be observed (Fig. 5). However, in Ni vs Fo space, the diffusion trends calculated for the different crystal habits at identical D_{Ni}/D_{Fo} ratios are still very close (Fig. 4b). As in the case of the asymptotic model of Newton's cooling law, the diffusion trends of three considered models have a concave-down curvature (Fig. 4a and b, respectively); however, their concavities are still more pronounced.

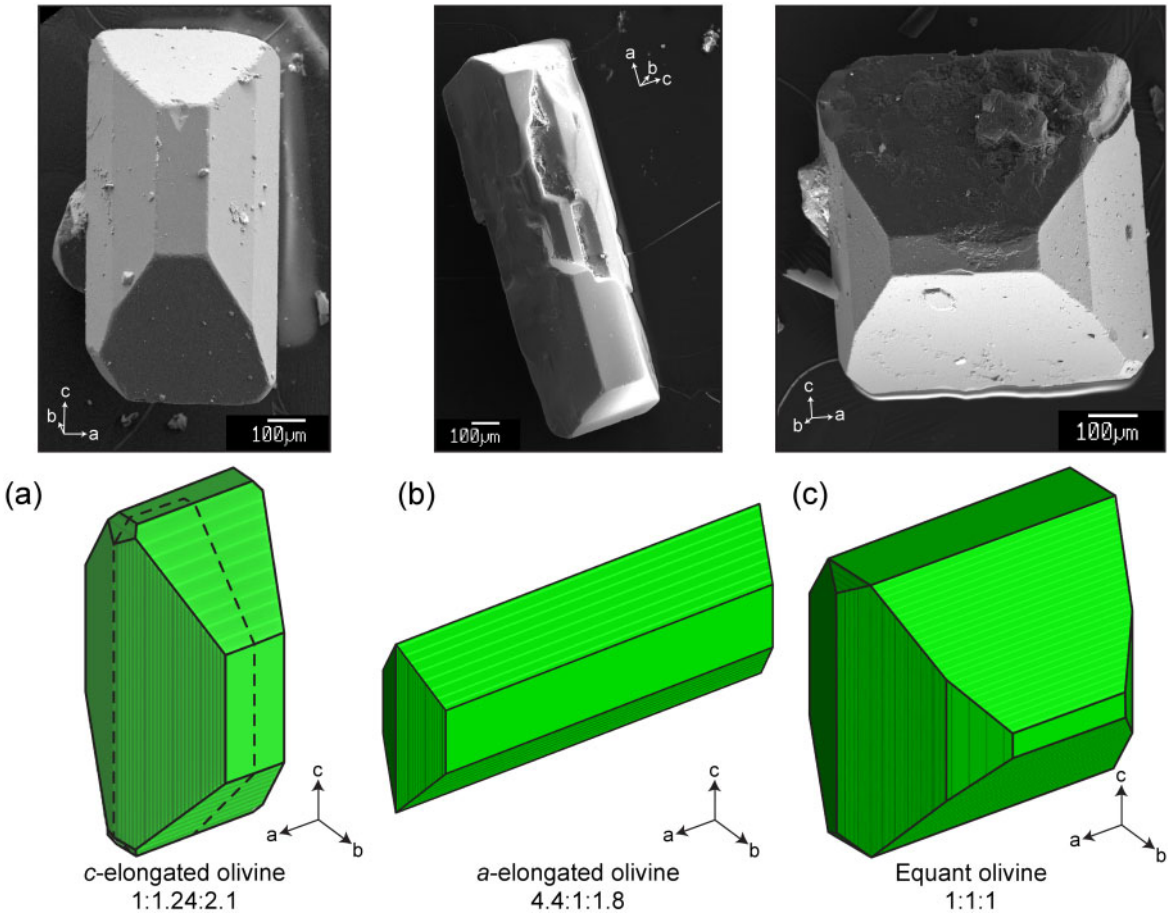

Fig. 6. Morphology of olivine crystals with realistic shapes used in 3D diffusion computational experiments. (a) Olivine crystal elongated along the *c*-axis, the most commonly found morphology in natural basalt. (b) Olivine crystal elongated along the *a*-axis. (c) The isometric olivine crystal (equant). For each olivine crystal, a secondary electron image (SEI) of a natural olivine is shown as a typical example (photographs courtesy of Jiyoung Heo).

Variations in the shapes of the diffusion trends (Fig. 4) can be explained as follows. In the case of a spherical model, the diffusion losses are strongest and identical in the three independent directions (Fig. 5), and the resulting diffusion trend is the most concave-down of the group. For a plane sheet the diffusion fluxes have only one direction, meaning that the curvature of the diffusion trend is least concave-down. The cylindrical model, with diffusion fluxes in two directions, occupies an intermediate position.

We conclude that for all considered models, crystal habit exerts only a limited influence on the shape of the diffusion trends.

The effect of anisotropy

Diffusion equation in an anisotropic olivine [equation (1)] can be written in Cartesian coordinates *x*, *y*, and *z* directed along the principal crystallographic axes *a*, *b*, and *c*:

$$\frac{\partial C}{\partial t}=\frac{\partial}{\partial x}D_{\mathrm{C}}^{a}\frac{\partial C}{\partial x}+\frac{\partial}{\partial y}D_{\mathrm{C}}^{b}\frac{\partial C}{\partial y}+\frac{\partial}{\partial z}D_{\mathrm{C}}^{c}\frac{\partial C}{\partial z}. \tag{20}$$

Because diffusivity is different only in the *z* direction (*c*-axis) compared with the *a*- and *b*-axes for Fo and Ni in olivine (Costa & Chakraborty, 2004; Chakraborty, 2010), we can use an analogue heat conductivity equation in an anisotropic solid (Carslaw & Jaeger, 1959) and transform the *z*-coordinate into a new variable z_*, using the coefficients from equation (4):

$$z_*=\sqrt{\frac{D_{\mathrm{C}}^{a}}{D_{\mathrm{C}}^{c}}}z=\frac{z}{\sqrt{6}} \tag{21}$$

which yields the same final form for the diffusion equation as for the isotropic medium:

$$\frac{\partial C}{\partial t}=\frac{\partial}{\partial x}D_{\mathrm{C}}^{a}\frac{\partial C}{\partial x}+\frac{\partial}{\partial y}D_{\mathrm{C}}^{a}\frac{\partial C}{\partial y}+\frac{\partial}{\partial z_*}D_{\mathrm{C}}^{a}\frac{\partial C}{\partial z_*}. \tag{22}$$

The *z*-coordinate in the initial and boundary conditions should also be transformed according to equation (21). Consequently, the problem of the losses of a chemical component from an olivine crystal with anisotropic properties [equation (4)] is reduced to the problem of component losses in an isotropic crystal

[equation (22)]; however, reduced by $\sqrt{6}$ times along the *c*-axis. In this fashion, the question about the effect of anisotropy on the diffusion trend is reduced to the question about the influence of the shape of isotropic crystals on the diffusion trend; that is, to the problem considered in the previous section. For example, an isometric olivine with anisotropic diffusion will produce the same diffusion trend as an isotropic crystal compressed by $\sqrt{6}$ times; that is, a crystal of approximately tabular habit.

Diffusion trends for natural olivine phenocryst shapes

Additional 3D numerical models of Fo–Ni diffusion in olivine were also carried out using several realistic morphologies typical in nature (Fig. 6) to test whether variations in crystal shape had an effect on the concave-down diffusion trends predicted for simpler crystal geometries. Previous studies utilized 3D diffusion models to explore the effects of sectioning, diffusion anisotropy, and crystal shape on zoning patterns and timescales recovered (Costa & Chakraborty, 2004; Costa *et al.*, 2008; Shea *et al.*, 2015*a*), and have been applied recently to case studies of Fo, Ni and Mn diffusion in olivine from Hawaiian basalt (Shea *et al.*, 2015*b*; Lynn *et al.*, 2017*b*). Similar models are employed herein to characterize Fo and Ni losses in the olivine; the diffusion time is long enough to significantly affect the concentration of both elements in the core.

Several different characteristic olivine morphologies were tested, using geometric aspect ratios A:B:C and anisotropic diffusion coefficients [equation (4)]: a classical *c*-elongated olivine, an *a*-elongated olivine, and an equant olivine (Fig. 6a–c). The choice of these three representative morphologies was made based on previous studies of experimental and natural olivine (Donaldson, 1976; Faure *et al.*, 2003, 2007; Deer *et al.*, 2013; Welsch *et al.*, 2013; Shea *et al.*, 2015*a*; Lynn *et al.*, 2017*a*; Mourey & Shea, 2019). The crystals with these morphologies were used as initial matrices for the numerical 3D anisotropic diffusion models with equation (20). Initial concentration in the crystal C_0 was set as unity, and concentration on the boundary C_m as zero.

Equation (20) was then solved using explicit finite differences; the details of the method used have been described by Shea *et al.* (2015*a*, 2015*b*) and Lynn *et al.* (2017*b*) and the changes in concentration at the centre of the core were tracked through time (Fig. 7).

Diffusion relationships between Fo and Ni extracted from the numerical 3D models were obtained from a single computed solution using the parametric representation equations (18) and (19). The resulting diffusion trends for variable D_{Ni}/D_{Fo} ratios were then compared with analytical models for different crystal habits (Fig. 4b).

The close correspondence between the diffusion trends of a classical *c*-elongated anisotropic olivine crystal (Fig. 6a) and the isotropic spherical models is related to the aspect ratio (1:1·24:2·1) of *c*-elongated olivine shape. Transforming the classical olivine along its *c*-axis in accordance with equation (21) would yield an effective aspect ratio of 1·17:1·45:1, which is not so far from an isometric model (Fig. 4b). In other words, the doubling of crystal dimension along the *c*-axis is nearly compensated by the six-fold diffusion anisotropy, which induces a $\sqrt{6} \approx 2{\cdot}4$ difference in diffusion length scale.

By comparison, the transformation of the *a*-elongated olivine (Fig. 6b) along the *c*-axis with equation (21) would result in 6:1·36:1 aspect ratio, similar to that of the cylinder, flattened from the sides. In full accordance with these observations, the diffusion trend of the *a*-elongated olivine phenocryst first starts between the trends followed by the cylindrical and plane sheet models, and then merges with the trend formed by the cylindrical model.

The equant olivine (Fig. 6c) would have an aspect ratio of 2·45:2·45:1 after being re-dimensionalized along the *c*-axis with equation (21). Indeed, the diffusion trend starts near the trend of the plane sheet model and then merges with the trend of the other models.

Thus, the diffusion trends of the anisotropic olivine crystals with complex, realistic morphology turn out to be completely inside the region bounded by the diffusion trends of the spherical model and the plane sheet model. This behaviour of the trends obtained in computational experiments fully corresponds to the results of theoretical analysis. It can be concluded yet again that it is the diffusivity ratio D_{Ni}/D_{Fo} that exerts the dominant control on the nature of the diffusion trend, and variably different realistic shapes have little bearing on the relationship between Fo and Ni (Fig. 4b).

DISCUSSION OF NATURAL EXAMPLES

Contrasting Fo–Ni diffusion trends in natural olivine crystals

In the following sections, we consider natural examples of concave-down Fo–Ni diffusions trends that we observed in olivine phenocrysts from rocks of two centres at Shiveluch volcano, a lava field near Bulochka and Novograblenov sub-synchronic monogenetic cones on the NE slope of Klyuchevskoy volcano, a high-Mg picritic basalt from Avachinsky volcano, and a lava flow from Zarechny stratovolcano. The analytical methods for these measurements are described above and have been described earlier by Gordeychik *et al.* (2018), and the full dataset is available in Supplementary Data Tables SM-1–4. We also present additional published examples of diffusion trends in olivine from mafic alkaline magmas from non-subduction settings from other studies.

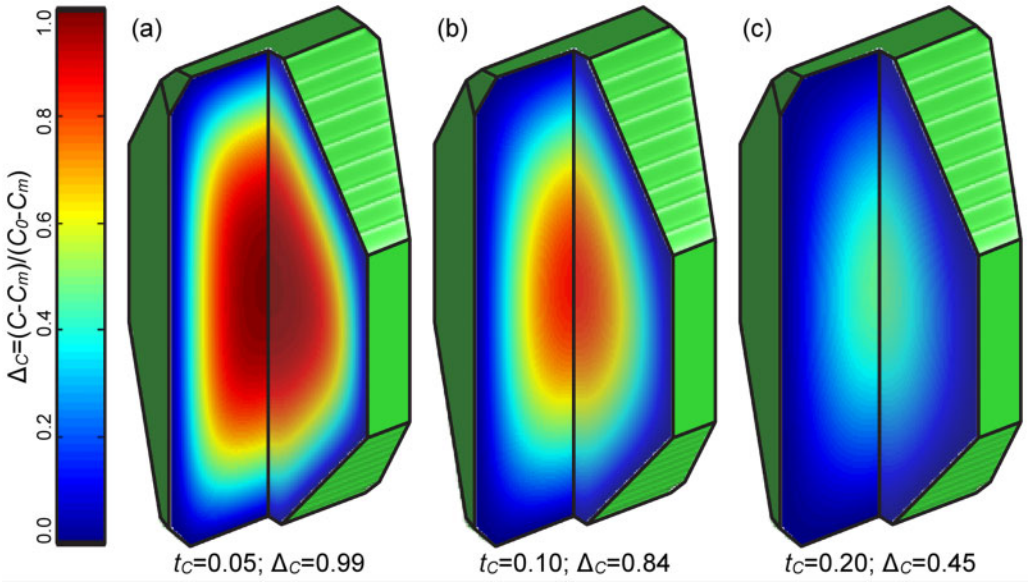

Fig. 7. Example model outputs in 3D cross-sections of *c*-elongated olivine crystals for different diffusion times t_C. Color represents non-dimensional concentration of a diffusing component. (a) The concentration of the component in the olivine core is almost unchanged from the initial concentration ($C = 0{\cdot}99$ of initial concentration). (b) The concentration in the olivine core has already been affected ($C = 0{\cdot}84$). (c) After time $t_C = 0{\cdot}2$, the concentration in the core is less than half of the initial value ($C = 0{\cdot}45$).

Diffusion trends in olivine phenocrysts from mafic arc magmas (Kamchatka)

Magnesian middle-K andesites and basaltic andesites with SiO_2 >55% are the main eruptive products of Shiveluch volcano during Holocene time, whereas rocks with SiO_2 <54% are extremely rare. Only two high-Mg basaltic tephra layers were found: one is moderately K-rich with age 7600 BP and the other is high-K with an age of 3600 BP (Volynets *et al.*, 1997).

Strongly zoned olivine phenocrysts were studied in a middle-K ol–cpx–pl basaltic clast ($SiO_2 = 52{\cdot}62$–$53{\cdot}74$ wt%, $K_2O = 0{\cdot}89$–$0{\cdot}92$ wt% after Churikova *et al.*, 2010; Nekrylov *et al.*, 2018), which was sampled from a 7600 BP maar deposit on the SW flank of Shiveluch volcano. Two contrasting trends were observed in these zoned olivine crystals (Gordeychik *et al.*, 2018): crystal rims form a steeply concave-up trend related to fractional crystallization from the host melt, whereas cores follow a slightly concave-down trend (Fig. 8a). The diffusion model matches the trend formed by the cores of individual crystals for a D_{Ni}/D_{Fo} ratio of 0·86. The diffusion origin of this compositional trend in olivine cores is supported not only by the curvature of trends in the Fo–Ni diagram (Fig. 8a) but also by compositional profiles through the olivine cores (Gordeychik *et al.*, 2018).

Another set of olivine crystals from a high-K ol–cpx–hbl–phl basalt ($SiO_2 = 51{\cdot}08$–$51{\cdot}51$ wt%, $K_2O = 1{\cdot}87$–$1{\cdot}9$ wt%; after Gorbach & Portnyagin, 2011; Nekrylov *et al.*, 2018) related to the eroded Shiveluch dike with the age 3600 BP shows similar diffusion trends in their cores indicating a comparable D_{Ni}/D_{Fo} of 0·96 (Fig. 8b) and subsequent crystallization trends in the rims.

A third set of data was obtained on olivine crystals from a high-Mg arc basalt ($SiO_2 = 50{\cdot}84$–$51{\cdot}43$ wt%, $MgO = 11{\cdot}0$–$12{\cdot}1$ wt%, $K_2O = 0{\cdot}5$–$0{\cdot}85$ wt% after Ariskin *et al.*, 1995; Ozerov, 2000; Churikova *et al.*, 2001) that was erupted at 2650 BP (V. V. Ponomareva, personal communication) from two adjacent vents on the lower NE slope of Klyuchevskoy volcano (Bulochka and Novograblenov scoria cones). The cores and the rims of the olivine phenocrysts again display different trends (Fig. 8c). Reasonable model fits through the trends of the olivine cores are obtained using $D_{Ni}/D_{Fo} = 0{\cdot}98$.

In contrast to the samples above, olivine cores from a high-Mg diopside-rich picritic basalt from Avachinsky volcano (Portnyagin *et al.*, 2005) first follow a crystallization trend and then are displaced from it to the left by diffusion (Fig. 8d) indicating a combination of crystallization and diffusion. Comparable shifts off the crystallization trend as a result of diffusion are observed in subsets of olivine crystals from samples of successively erupted tephra from Paricutin volcano (supplementary data fig. S12 of Albert *et al.*, 2020). Another example of the combination of these two processes can be seen in olivine compositions from Zarechny volcano lava flow (Fig. 8e). A crystallization trend is formed by only a part of olivine cores; other cores deviate from the crystallization trend and are probably controlled by diffusion with $D_{Ni}/D_{Fo} = 0{\cdot}75$.

The examples shown in Fig. 8 alone cannot constrain a diffusion trend formed by Ni-enriched olivine cores. The point here is that the diffusion model for Ni-enriched olivine crystals is demonstrated in the model and also with other, more convincing datasets from natural occurrences, where diffusion-modified cores can

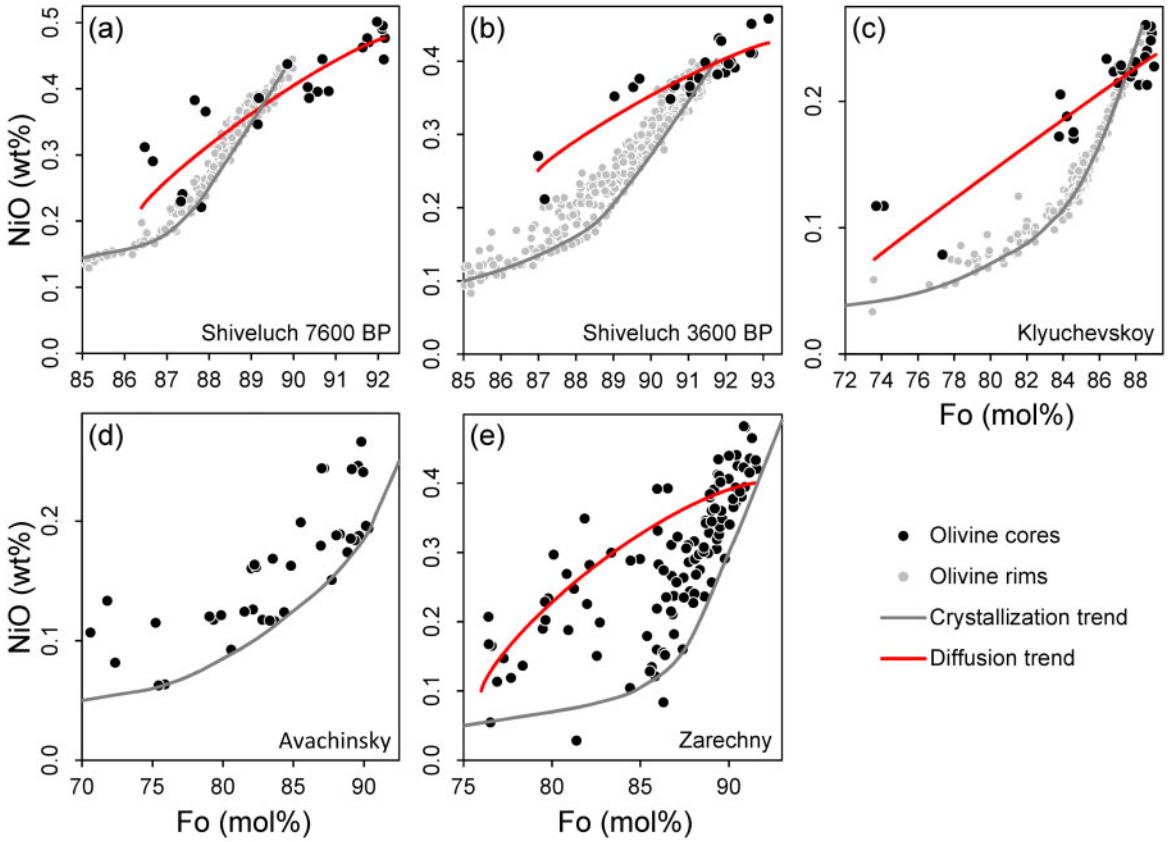

Fig. 8. Fo–Ni diagrams for olivine compositions from lavas erupted in a subduction setting: (a) 7600 BP tuff ring on Shiveluch volcano after (Gordeychik *et al.*, 2018); (b) 3600 BP high-K basaltic dyke on Shiveluch volcano; (c) Bulochka and Novograblenov cones on the flank of Klyuchevskoy volcano; (d) high-Mg picritic basalt from Avachinsky volcano; (e) lava flow from Zarechny volcano. In all diagrams, black dots represent olivine core compositions and grey circles are olivine rims. The red lines show concave-down diffusion trends, calculated from an analytical solution using the least-squares method. Grey lines indicate the concave-up crystallization trends.

be better distinguished from the 'normal' fractional crystallization trend. Then, understanding what protracted diffusion does with Fo and Ni compositions of olivine cores, individual outliers such as those in Fig. 8b (and many other examples where such outliers have been observed) can now be identified and be explained by diffusion.

Despite slightly variable concavity of the diffusion trends and variable slopes of crystallization trends, the high-Ni trends and high-Ni outliers from crystallization trends documented here show that the concave-down trends formed by the olivine cores contrast sharply with the direction and curvature of (rim) crystallization trends. The concavity of the trend inferred for olivine cores is low when values of D_{Ni}/D_{Fo} are close to unity (0·86–0·98). In this case, the trends in the Fo–Ni diagram are inconclusive because, in principle, such a trend could also form when mixing of crystal-free magmas is considered, followed by nucleation and crystallization of olivine (Straub *et al.*, 2008; Gleeson & Gibson, 2019). In the latter scenario, olivine crystallization after mixing would result in series of steep trends shifted to lower Fo at almost constant Ni composition. However, steep Fo–Ni trends displaced to higher fayalite are not observed. Given this constraint, simple continuous crystallization from fayalite-rich and Ni-rich melt cannot explain the observed trends in the Fo–Ni diagram (Fig. 8). We conclude that complete or partial Fo–Ni homogenization of olivine cores through diffusion has occurred in all the examples studied here.

Gordeychik *et al.* (2018) showed that Fo–Ni zoning trends in the olivine cores from the 7600 BP Shiveluch eruption were smoothed by diffusion to a variable extent. An example of complete Fo–Ni homogenization in the core of an olivine from the basalt of the NE slope of Shiveluch volcano is given in Fig. 9. The COMPO image (Fig. 9a) shows a large (3 mm long) olivine with a homogeneous core in Fe–Mg and Ni (Fig. 9f–h). Element maps for slower diffusing elements such as Ca, Al, and Cr (Fig. 9c–e) show a variably triangular olivine core (0·5 mm) that is not visible in Fe, Mg, or Ni maps. The primary, triangle-shaped core and the surrounding olivine have therefore been completely homogenized in the faster-diffusing elements.

Our data thus indicate that diffusion can dramatically change the composition of olivine, not only at the rims of crystals, but also inside their cores. Identifying the complete history of olivine crystallization and diffusion,

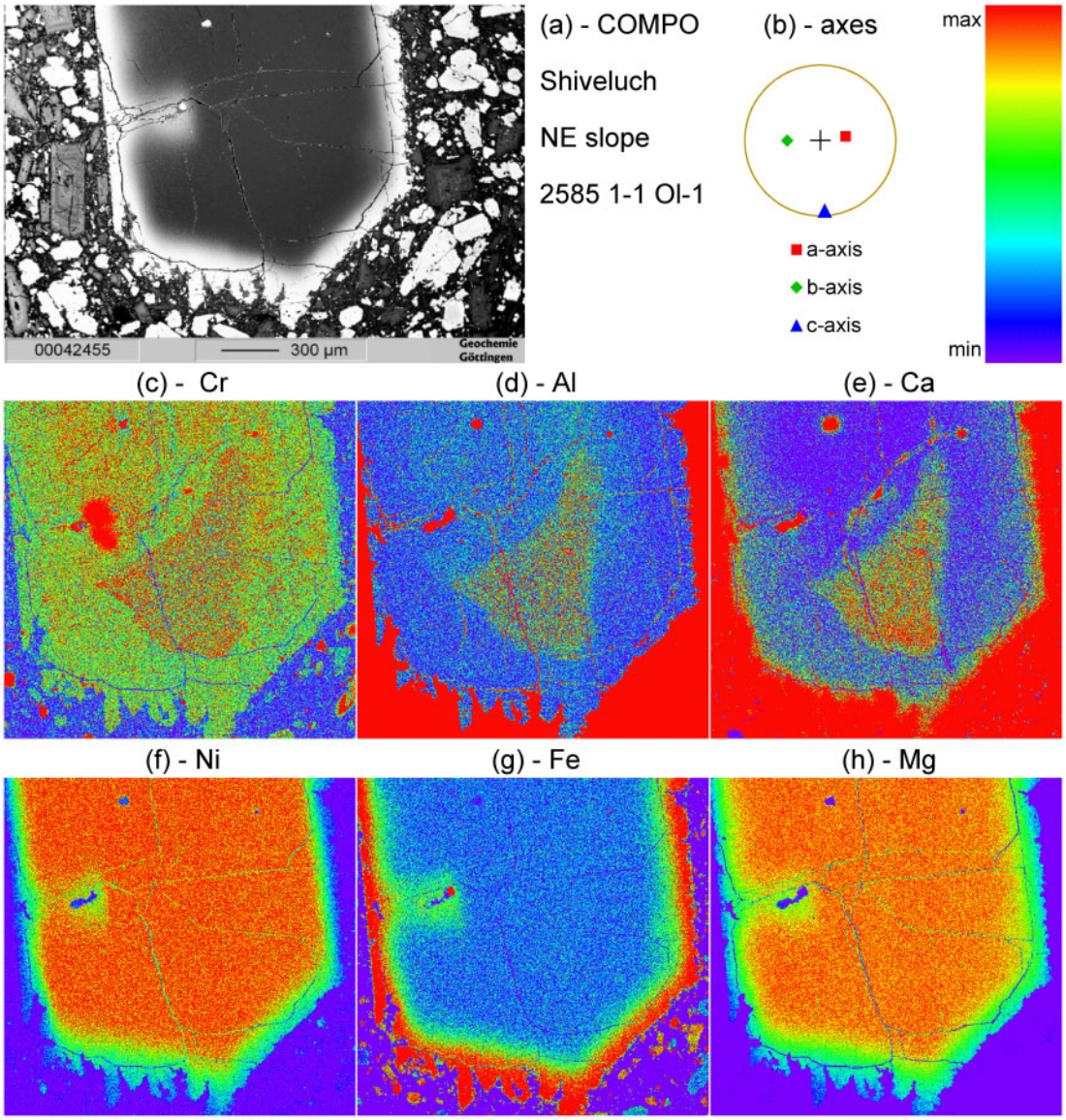

Fig. 9. (a) COMPO image of olivine crystal from a basaltic lava flow on the NE slope of the Shiveluch volcano. (b) Projections of *a*-, *b*-, and *c*-axes of crystals shown in a stereographic lower hemisphere plot. (c–e) The core shows an irregular shape that is visible only in element maps of low-diffusing Cr, Al, and Ca. (f–h) The core is completely homogeneous for fast-diffusing Ni, Fe and Mg. Analytical methods for element mapping were as described by Gordeychik *et al.* (2018).

including their cores, may hold important clues about their origin.

These examples also show that only rapidly ascending mafic magmas with short mixing-to-eruption timescales allow records of preservation of both crystallization and diffusion, which can be distinguished as complex patterns in the Fo–Ni diagram. This is because preserving such patterns requires relatively rapid crustal transfer from deep magmatic reservoirs where mixing occurs between primitive and more evolved magmas prior to eruption. If post-mixing storage or magma transfer times at high temperature are protracted, initial compositional variations in Fo and even Ni may be completed erased in olivine cores, in which case this record can be lost completely.

Both rapid and protracted mixing-to-eruption timescales are shown in Fig. 10, where the ascent timescales recorded by of olivine crystals is compared with their homogenization time. The mixing-to-eruption timescales for these eruptions are extracted from literature data (Costa & Dungan, 2005; Qian *et al.*, 2010; Lynn *et al.*, 2017*b*; Gordeychik *et al.*, 2018; Sundermeyer *et al.*, 2020) and considered here to represent an equivalent integrated transfer time to the surface. The homogenization time is plotted as a function of temperature using equation (14) for four characteristic sizes of olivine crystals, and for thermodynamic conditions relevant to each eruption. For eruptions that preserved core Fo–Ni variations (Shiveluch 7600 BP, Shiveluch 3600 BP, Klyuchevskoy high-Mg basalts), the recorded mixing to

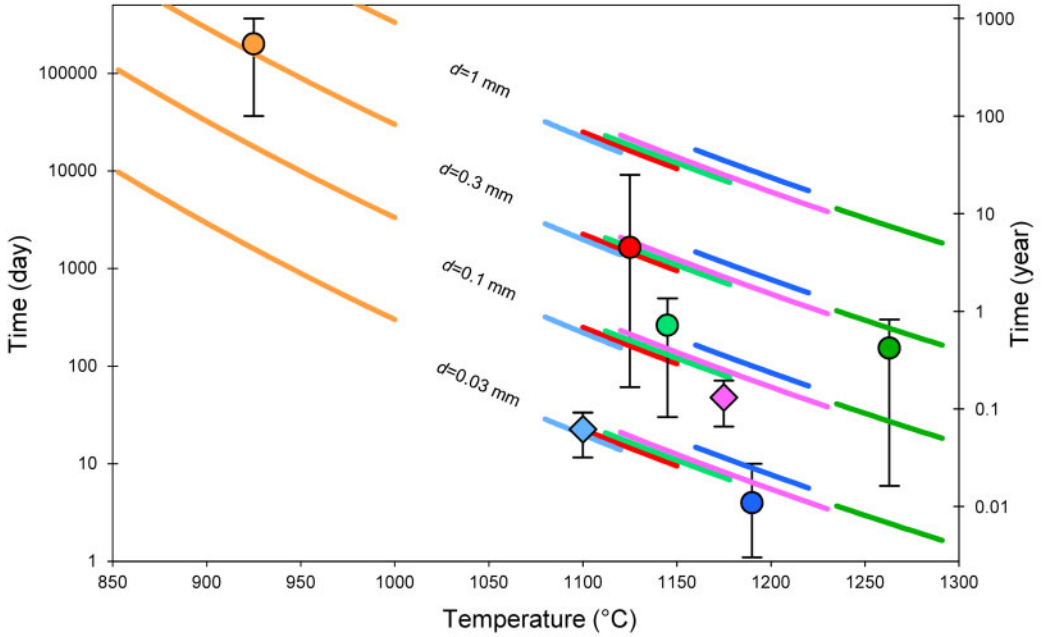

Volcano studied	Average mixing-to-eruption timescales (day or year)	Number of time estimates	Compositional and thermodynamic conditions				Relaxation time (day or year)
			Fo (mol%)	Temperature interval (°C)	Pressure (bar)	Fugacity buffer	
Tatara-San Pedro (Costa & Dungan, 2005)	●	57	82	1100-1150	3000	NNO	
Handan-Xingtai (Qian *et al*., 2010)	●	2	91	850-1000	4000	QFM+0.75	
Kīlauea (Lynn *et al*., 2017a)	●	68	85	1235-1291	850	QFM	
Piton de la Fournaise (Sundermeyer *et al*., 2020)	●	44	82	1112-1178	1000	NNO-0.5	
Shiveluch 7600 BP (Gordeychik *et al*., 2018)	●	9	90	1160-1220	8000	QFM+1	
Shiveluch 3600 BP (this study)	◆	2	86	1080-1020	8000	QFM+2.1	
Klyuchevskoy, high-Mg basalt (this study)	◆	2	87	1120-1230	7500	QFM+1.3	

Fig. 10. Comparison of the mixing-to-eruption times determined from Fo-diffusion modelling of zoned olivine phenocrysts for different natural examples and homogenization times calculated here for olivine phenocrysts of various size. Colored symbols with error bars indicate average ascent timescales and the average of the absolute deviations; the number of estimates in each example is shown in the legend. Colored curves show the homogenization time calculated here [equation (14)] using Fo diffusion coefficient defined by Chakraborty (2010) under compositional and thermodynamic conditions as documented in the corresponding papers given in the legend. The four sets of curves correspond to olivine phenocrysts of different characteristic sizes from 0·03 to 1 mm.

eruption time is shorter than, or comparable with, the homogenization time of small olivine crystals. The remaining eruptions preserve longer timescales comparable with the homogenization time of large olivine phenocrysts. This situation can be likened to photographing moving objects: if the exposure time is short compared with the characteristic time of the object's movement, a clear picture will be obtained. In the case of short mixing-to-eruption times, the Fo–Ni variations are conserved by all crystals. If mixing-to-eruption times are long, Fo–Ni variations can be erased or distorted in most crystals depending on their size, and only the largest crystals will conserve the primary Fo–Ni distribution in their core. It should be noted that the shortest mixing-to-eruption time was observed for the 7600 BP Shiveluch phreatomagmatic maar eruption, so complex Fo–Ni olivine trends and the olivine phenocrysts with a strong zoning are most pronounced and were not erased by diffusion in these rocks. As for all considered natural examples, only olivine with size 1 mm and more can retain the primary Fo–Ni distribution.

The rarity of such complex Fe, Mg and Ni zoning patterns in most olivine cores may be due to relatively long storage, magma migration and mixing timescales at high temperatures to allow for preservation of recorded compositional gradients. This implies that diffusion processes can profoundly change olivine core compositions and erase complex zoning patterns, and this may be the rule rather than the exception. Only high ascent rates and limited timescales of diffusion, as inferred for our examples, can preserve primary core zoning patterns in olivine.

Diffusion trends in olivine phenocrysts from lamproites and kimberlites

Highly alkaline mafic magmas, such as lamproites and kimberlites, are also inferred to ascend rapidly, driven by early CO_2 degassing at depth. Complex Ni-enriched compositional trends deviating from, but combined with, predicted crystallization trends were also described in olivine phenocrysts from lamproitic and kimberlitic lavas, in agreement with our interpretations.

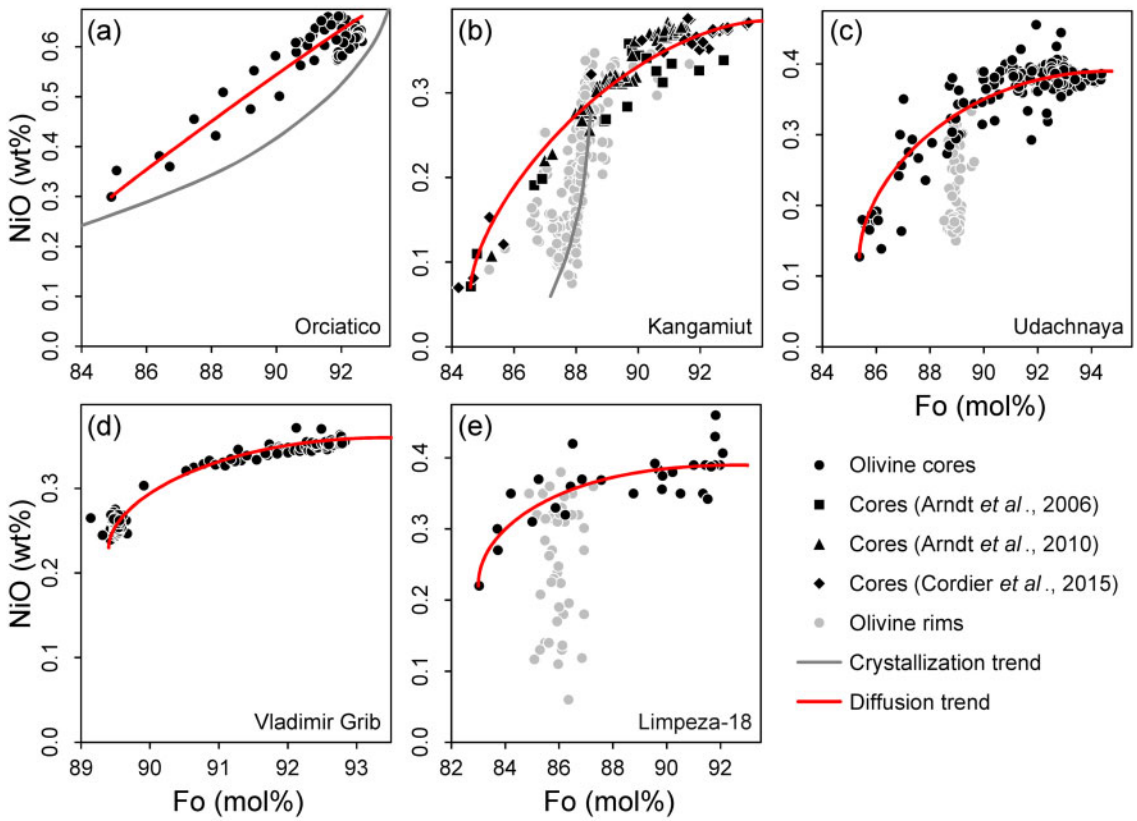

Fig. 11. Fo–Ni diagrams for the olivine compositions in natural samples from non-subduction settings: (a) lamproitic lavas from Orciatico, Italy (Prelević *et al.*, 2013); (b) a kimberlite dyke from the Kangamiut region in West Greenland, with squares, triangles, and circles marking different data sources (Arndt *et al.*, 2006, 2010; Cordier *et al.*, 2015) for the same sample material; (c) Udachnaya-East kimberlite pipe from the Daldyn–Alakit province, Yakutia, northern Siberia, Russia (Kamenetsky *et al.*, 2008, 2011); (d) Vladimir Grib kimberlite pipe, Arkhangelsk Diamond Province, Russia (Sazonova *et al.*, 2015; Kargin *et al.*, 2017); (e) Limpeza-18 kimberlite, Alto Paranaiba Igneous Province, Brazil (Lim *et al.*, 2018). Black circles show the concave-down diffusion trends formed by olivine cores. Grey circles are olivine rim compositions that form steep trends of the final stage of crystallization from a host melt. For (a) and (b), grey lines show the trend of the final crystallization stage after Prelević *et al.* (2013) and Cordier *et al.* (2015) respectively. Red lines represent concave-down diffusion trends, calculated by an analytical solution using least squares.

Prelević *et al.* (2013) documented the concave-up curvature of the crystallization trend in olivine crystals from Orciatico, Italy (Fig. 11a) to contrast with the near-linear trend formed by the olivine cores, which can be approximated by a diffusion model with $D_{Ni}/D_{Fo} = 0{\cdot}97$.

Figure 11b–e shows additional characteristic Fo–Ni trends in olivine crystals for other examples: a kimberlite dike from the Kangamiut region, West Greenland (Arndt *et al.*, 2006, 2010; Cordier *et al.*, 2015); the kimberlite pipe Udachnaya-East, Yakutia, Russia (Kamenetsky *et al.*, 2008, 2011); a garnet peridotite from the Vladimir Grib kimberlite pipe, Arkhangelsk Diamond Province, Russia (Sazonova *et al.*, 2015; Kargin *et al.*, 2017); and the kimberlite pipe Limpeza 18, Alto Paranaiba Igneous Province, Brazil (Lim *et al.*, 2018). In all these cases, the olivine cores form concave-down trends that are in good agreement with diffusion trends. D_{Ni}/D_{Fo} values derived from the models are lower (0·64, 0·54, 0·53 and 0·48) than the diffusion coefficients ratios obtained above for olivine from subduction zones. The absolute value of D_{Ni}/D_{Fo} probably depends on differences in P–T–fO_2 conditions for these different settings.

We conclude from these examples and our previous reasoning that olivine phenocrysts from fast ascending magmas—either in an arc setting or from intraplate setting (kimberlites, lamproites)—can indeed record Fo–Ni diffusion trends in their cores (Fig. 11a and d) that are distinct from trends that may form on such cores as overgrowths by fractional crystallization (Fig. 11b, c, and e).

Our theoretical diffusion trends were obtained under the assumption that changes in olivine composition are minor. Despite the wide ranges in forsterite for Shiveluch basalts ($Fo_{87–92}$), Klyuchevskoy and Zarechny rocks ($Fo_{75–90}$), and intraplate rocks ($Fo_{84–93}$), our models adequately describe the concave-down diffusion trends arising in natural environments (Figs 8 and 11).

Coupled fractional crystallization and diffusion processes

In natural olivine, diffusion and fractional crystallization could potentially occur simultaneously or in sequence in complex mixing–cooling–crystallization scenarios, and this will govern the overall variation of olivine compositions. These processes would be particularly

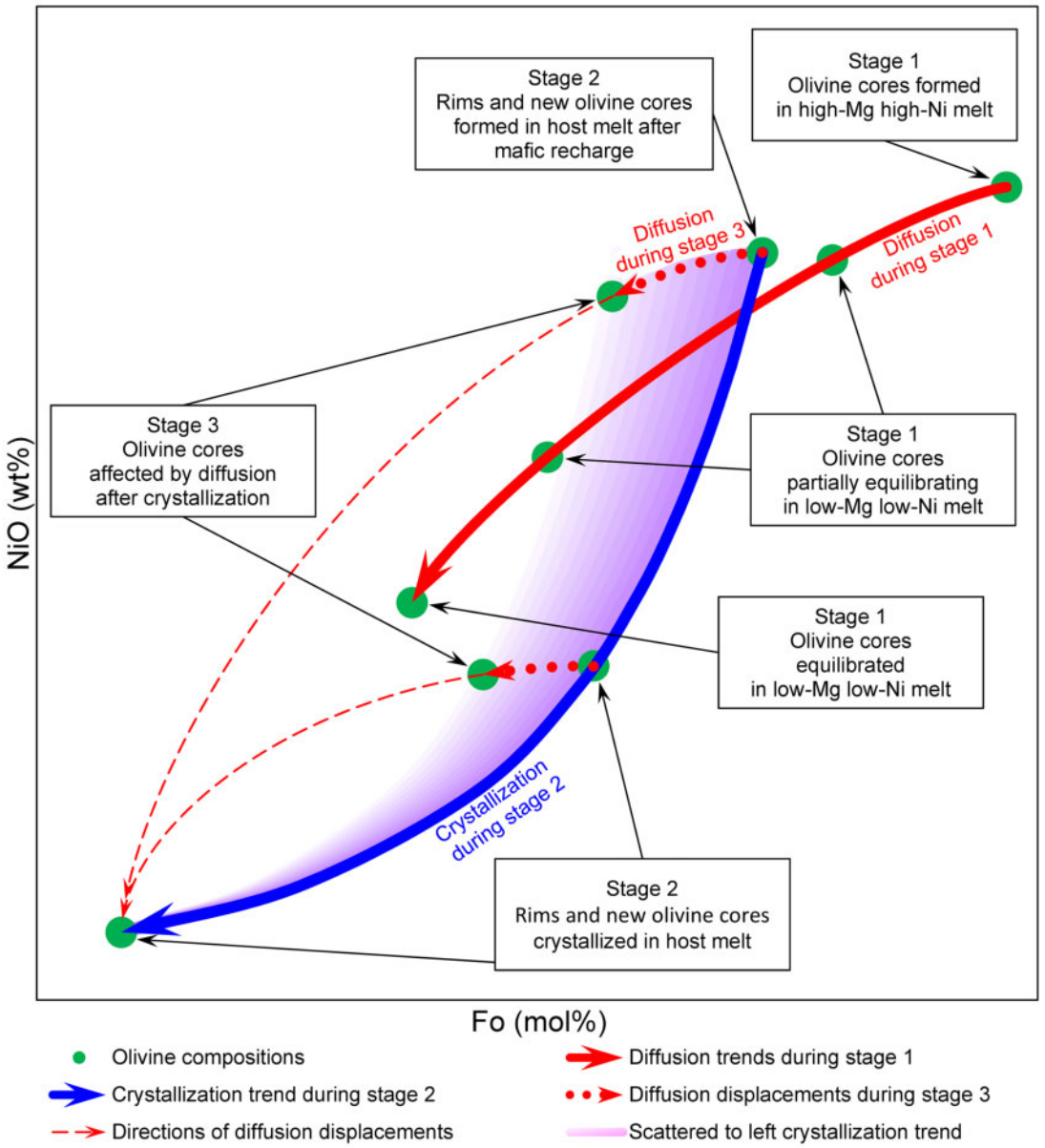

Fig. 12. Schematic diagram showing possible combinations of crystallization and diffusion trends (for explanation see text).

difficult to distinguish if magma mixing occurs at intermediate stages of evolution with little compositional contrast between mixing endmembers. In other cases, diffusive equilibration or fractional crystallization could occur in a closed system and without significant mixing. The effects of these contrasting endmember processes and combinations thereof on Fo–Ni trends are depicted schematically in Fig. 12 and this forms the backbone of our interpretations based on the natural examples. We deliberately did not include possible processes other than diffusion and crystallization (e.g. mixing or oxidation) in Fig. 12. Such additional processes undoubtedly can have effects, as discussed above. However, for the sake of clarity in the presentation of the effects of diffusion versus crystallization, these processes were omitted.

Stage 1. Initial olivine cores all crystallize with similar compositions from a high-Mg, high-Ni melt. This olivine is then mixed into a low-Mg, low-Ni melt. Diffusion will modify the olivine cores along the continuous red diffusion trend in Fig. 12 until the olivine cores are partly or fully equilibrated with a low-Mg, low-Ni melt.

Stage 2. After renewed mafic recharge new olivine cores as well as rims on pre-existing older olivine cores from Stage 1 crystallize with an intermediate composition after mixing. This growth occurs by fractional crystallization during storage and/or ascent within a host hybrid melt. Whatever the earlier diffusion history may be, crystallization from the new hybrid host melt could start at any time, at any intermediate composition, which determines the point at which the fractional crystallization path initiates (blue line in Fig. 12). The

intersection between trends of diffusion and fractional crystallization (Figs 8, 11, and 12) then can occur at different angles and for different Fo–Ni contents. The point of intersection between the diffusion trend (red line) and the crystallization trend (blue line) reflects the starting composition of new olivine rims that will crystallize from the hybrid melt on a range of older crystal cores (green points on the red line).

Stage 3. At any stage new olivine phenocrysts formed by fractional crystallization may again experience disequilibrium conditions with a more evolved melt. If diffusion times are long, this results in displacements from the crystallization trend to the left (dotted red diffusion trends in Fig. 12) towards a new equilibrium (dashed red lines in Fig. 12). Such combined crystallization–diffusion processes can explain the scatter to the left from the crystallization trends that is often observed in natural examples (Fig. 8d and e).

We conclude that combined diffusion and fractional crystallization may occur in natural examples of olivine phenocrysts and that these processes can be combined in different ways, yielding a variety of patterns of olivine distributions (Figs 8 and 11). For example, the absence of stage 1 could yield zoning characteristics akin to olivine from Avachinsky volcano (Fig. 8d), or the absence of stage 3 could yield a core and rim distribution similar to olivine from Shiveluch (Fig. 8a). In the latter case, rims record the composition of melt during fractional crystallization (stage 2) and follow the blue line in Fig. 12. In the absence of both diffusion stages (1 and 3), we will observe only a simple trend of fractional crystallization. In the presence of diffusion, older cores may be significantly changed and may be observed next to younger olivine populations that are later formed only by fractional crystallization. Moreover, olivine cores can be obtained both from a high-Mg, high-Ni melt (Fig. 12) and from xenocrystic olivine that could be entrained from disintegrated peridotite mantle rocks. Thus, understanding the nature and controls of the diffusion trend and its contrast to the trend of fractional crystallization allows us to better understand patterns of olivine Fo–Ni distributions in mafic magmatic rocks and to reconstruct their provenance and pre-eruptive histories.

CONCLUSIONS

This contribution presents the effects of protracted Fo and Ni diffusion in the cores of olivine crystals after being immersed in more evolved melt. It is shown that, for an olivine population of a given sample at certain P–T–fO_2 conditions, all crystals pass along approximately the same Fo–Ni diffusion trajectory, which connects the high-Fo and high-Ni olivine compositions to its equilibrium with more evolved melt. The study and analysis of these diffusion trends allow the following conclusions.

(1) Natural olivine phenocrysts that were not fully equilibrated and preserve a record of the diffusion history and diffusion trends suggest that D_{Ni}/D_{Fo} should generally be smaller than unity.

(2) For $D_{Ni}/D_{Fo} < 1$, olivine cores define a diffusion trend that has a concave-down curvature in the Fo–Ni diagram, opposite to the concave-up crystallization trend.

(3) The analytical considerations of the diffusion equations show that different crystal habits and anisotropy have little effect on the curvature of the diffusion trends. The concave-down curvature of the diffusion trend is mainly controlled by the diffusion coefficient ratio D_{Ni}/D_{Fo}, whereas the initial and final trend points correspond to the initial composition of the olivine cores and equilibrium values in the evolved melt, respectively.

(4) Three-dimensional modelling for anisotropic diffusion in the olivine crystals of realistic shape shows that their diffusion trends lie between the diffusion trends of the spherical model and the plane sheet model; such behaviour of the calculated trends is in full agreement with theoretical considerations.

(5) The analytical and numerical diffusion models developed here yield Fo–Ni diffusion trends that are very close to each other for a given D_{Ni}/D_{Fo} ratio. Therefore, when investigating diffusion behaviour of two elements with different diffusivities, the effect of shape and anisotropy is smaller than uncertainties in element diffusivities and can be neglected.

(6) The diffusion may obscure the geochemical information about the origin and history of olivine crystals for fast-diffusing elements (e.g. Fo and Ni). On the other hand, the diffusion trends, when properly interpreted, may provide information about the initial melt composition and the more evolved melt after the mixing process. The curvature of the diffusion trend defines the ratio of Fo and Ni diffusion coefficients, which itself reflects the thermodynamics conditions during diffusion.

(7) Recognizing the stark contrast between diffusion and crystallization trends in Fo–Ni plots allows more detailed and robust interpretations of the history and evolution of magmas and their contained olivine crystals.

(8) Information on the genesis of olivine, recorded in Fo–Ni distributions of phenocrysts and in their zoned profiles, is erased when the ascent time of the crystals is longer than or comparable with their diffusion homogenization time. Fo–Ni information can be stored only if the ascent time is less than the diffusion homogenization time of the crystals.

ACKNOWLEDGEMENTS

We are grateful to Maria Pevzner for providing tephra sample 748/1 from the 3600 BP Shiveluch eruption and to Alexander Ovsyannikov for providing sample AVA-14-01 from Avachinsky volcano. We thank Jiyoung Heo for providing images of olivine phenocrysts from the Koko Head Tuff, Hawaii. Special thanks go to Ivan Savov, Rosie Jones, Lubomira Tomanikova, and Stephen Turner (Deep Volatiles Consortium, http://

www.deepvolatiles.org) for assistance during the fieldwork. The authors thank colleagues who supported in the organization of fieldwork: Yaroslav Muraviev, Valentina Fedulova, Oleg Bograd, Yury Demyanchuk, and Nadezhda Egorova. We appreciate contributions from our selfless volunteers who worked with us in Kamchatka: Elena Chesalova, Andrey Griban, Igor Lebedev, Natalya Melehina, Alexander Muraviev, and rescuer Mihail Yarin. We had very fruitful discussions with Natalia Gorbach, Maya Kopylova, Nikita Mironov, Georgy Nikolaev, Vera Ponomareva, and Maxim Portnyagin. Philipp Ruprecht and two anonymous reviewers performed a rigorous and critical review of the original paper, and Editor Adam Kent is also thanked for providing very helpful comments. As a result of their insights, the revised paper has been greatly improved.

FUNDING

This research was supported by Deutsche Forschungsgemeinschaft (DFG) grant No. Wo 362/51-1 and Russian Foundation for Basic Research (RFBR) grants Nos 16-55-12040, 17-55-50005 and 20-55-50001.

SUPPLEMENTARY DATA

Supplementary data are available at *Journal of Petrology* online.

REFERENCES

Albert, H., Larrea, P., Costa, F., Widom, E. & Siebe, C. (2020). Crystals reveal magma convection and melt transport in dyke-fed eruptions. *Scientific Reports* **10**, article number 11632.

Ariskin, A. A. & Barmina, G. S. (2004). COMAGMAT: development of a magma crystallization model and its petrological applications. *Geochemistry International* **42(Supplement 1)**, S1–S157.

Ariskin, A., Barmina, G., Ozerov, A. & Nielsen, R. (1995). Genesis of high-alumina basalts from Klyuchevskoi Volcano. *Petrology* **3**, 449–472.

Arndt, N. T., Boullier, A. M., Clement, J. P., Dubois, M. & Schissel, D. (2006). What olivine, the neglected mineral, tells us about kimberlite petrogenesis. *eEarth* **1**, 15–21.

Arndt, N. T., Guitreau, M., Boullier, A. M., Le Roex, A., Tommasi, A., Cordier, P. & Sobolev, A. (2010). Olivine, and the origin of kimberlite. *Journal of Petrology* **51**, 573–602.

Ballhaus, C., Berry, R. F. & Green, D. H. (1991). High pressure experimental calibration of the olivine–orthopyroxene–spinel oxygen geobarometer: implications for the oxidation state of the upper mantle. *Contributions to Mineralogy and Petrology* **107**, 27–40.

Batanova, V. G., Sobolev, A. V. & Kuzmin, D. V. (2015). Trace element analysis of olivine: High precision analytical method for JEOL JXA-8230 electron probe microanalyser. *Chemical Geology* **419**, 149–157.

Besson, U. (2011). The cooling law and the search for a good temperature scale, from Newton to Dalton. *European Journal of Physics* **32**, 343–354.

Bird, R. B., Stewart, W. E. & Lightfoot, E. N. (2002). *Transport Phenomena*. New York: John Wiley.

Bouvet de Maisonneuve, C., Costa, F., Huber, C., Vonlanthen, P., Bachmann, O. & Dungan, M. A. (2016). How do olivines record magmatic events? Insights from major and trace element zoning. *Contributions to Mineralogy and Petrology* **171**, 56.

Carslaw, H. S. & Jaeger, J. C. (1959). *Conduction of Heat in Solids*. Oxford: Clarendon Press.

Chakraborty, S. (2010). Diffusion coefficients in olivine, wadsleyite and ringwoodite. In: Zhang, Y. & Cherniak, D. J. (eds) *Diffusion in Minerals and Melts. Reviews in Mineralogy and Geochemistry. McLean, Va: Mineralogical Society of America and Geochemical Society,* **72**, 603–639.

Churikova, T., Dorendorf, F. & Wörner, G. (2001). Sources and fluids in the mantle wedge below Kamchatka, evidence from across-arc geochemical variation. *Journal of Petrology* **42**, 1567–1593.

Churikova, T. G., Gordeychik, B. N., Belousov, A. B. & Babansky, A. D. (2010). Find the centre of the eruption of basalts on the Volcano Shiveluch. In: Gordeev, E. I. (ed.) *Materials of All-Russian Conference Dedicated to the 75th Anniversary of the Kamchatka Volcanological Station. Petropavlovsk-Kamchatsky, September 9–15, 2010*. Petropavlovsk-Kamchatsky: Institute of Volcanology and Seismology FEB RAS, 102–105 (In Russian).

Cordier, C., Sauzeat, L., Arndt, N. T., Boullier, A.-M., Batanova, V. & Barou, F. (2015). Metasomatism of the lithospheric mantle immediately precedes kimberlite eruption: new evidence from olivine composition and microstructures. *Journal of Petrology* **56**, 1775–1796.

Cordier, C., Sauzeat, L., Arndt, N. T., Boullier, A.-M., Batanova, V. & Barou, F. (2016). The geochemical complexity of kimberlite rocks and their olivine populations: a Reply to the comment on Cordier *et al.* (2015) by Andrea Giuliani & Stephen F. Foley. *Journal of Petrology* **57**, 927–932.

Cordier, C., Sauzeat, L., Arndt, N. T., Boullier, A.-M., Batanova, V. & Barou, F. (2017). Quantitative modelling of the apparent decoupling of Mg# and Ni in kimberlitic olivine margins: a Reply to the comment on Cordier *et al.* (2015) by A. Moore. *Journal of Petrology* **58**, 391–393.

Costa, F. & Chakraborty, S. (2004). Decadal time gaps between mafic intrusion and silicic eruption obtained from chemical zoning patterns in olivine. *Earth and Planetary Science Letters* **227**, 517–530.

Costa, F. & Dungan, M. (2005). Short time scales of magmatic assimilation from diffusion modeling of multiple elements in olivine. *Geology* **33**, 837–840.

Costa, F. & Morgan, D. (2010). Time constraints from chemical equilibration in magmatic crystals. In: Dosseto, A., Turner, S. P. and Van-Orman, J. A. (eds) *Timescales of Magmatic Processes from Core to Atmosphere*. New York: John Wiley, pp. 125–159.

Costa, F., Dohmen, R. & Chakraborty, S. (2008). Time scales of magmatic processes from modeling the zoning patterns of crystals. In: Putirka, K. D. & Tepley III, F. J. (eds) *Minerals, Inclusions and Volcanic Processes. Reviews in Mineralogy and Geochemistry. McLean, Va: Mineralogical Society of America and Geochemical Society,* **69**, 545–594.

Crank, J. (1975). *The Mathematics of Diffusion*. Oxford: Oxford University Press.

Deer, W. A., Howie, R. A. & Zussman, J. (2013). *An Introduction to the Rock-Forming Minerals*. London: Mineralogical Society of Great Britain and Ireland.

Dohmen, R. & Chakraborty, S. (2007). Fe–Mg diffusion in olivine II: point defect chemistry, change of diffusion mechanisms and a model for calculation of diffusion coefficients in natural olivine. *Physics and Chemistry of Minerals* **34**, 409–430.

Dohmen, R., Becker, H.-W. & Chakraborty, S. (2007). Fe–Mg diffusion in olivine I: experimental determination between 700 and 1,200°C as a function of composition, crystal orientation and oxygen fugacity. *Physics and Chemistry of Minerals* **34**, 389–407.

Donaldson, C. H. (1976). An experimental investigation of olivine morphology. *Contributions to Mineralogy and Petrology* **57**, 187–213.

Faure, F., Trolliard, G., Nicollet, C. & Montel, J.-M. (2003). A developmental model of olivine morphology as a function of the cooling rate and the degree of undercooling. *Contributions to Mineralogy and Petrology* **145**, 251–263.

Faure, F., Schiano, P., Trolliard, G., Nicollet, C. & Soulestin, B. (2007). Textural evolution of polyhedral olivine experiencing rapid cooling rates. *Contributions to Mineralogy and Petrology* **153**, 405–416.

Girona, T. & Costa, F. (2013). DIPRA: A user-friendly program to model multi-element diffusion in olivine with applications to timescales of magmatic processes. *Geochemistry, Geophysics, Geosystems* **14**, 422–431.

Giuffrida, M. & Viccaro, M. (2017). Three years (2011–2013) of eruptive activity at Mt. Etna: Working modes and timescales of the modern volcano plumbing system from micro-analytical studies of crystals. *Earth-Science Reviews* **171**, 289–322.

Giuliani, A. (2018). Insights into kimberlite petrogenesis and mantle metasomatism from a review of the compositional zoning of olivine in kimberlites worldwide. *Lithos* **312–313**, 322–342.

Giuliani, A. & Foley, S. F. (2016). The geochemical complexity of kimberlite rocks and their olivine populations: a comment on Cordier. *Journal of Petrology* **57**, 921–926.

Gleeson, M. L. M. & Gibson, S. A. (2019). Crustal controls on apparent mantle pyroxenite signals in ocean-island basalts. *Geology* **47**, 321–324.

Gorbach, N. V. & Portnyagin, M. V. (2011). Geology and petrology of the lava complex of Young Shiveluch Volcano. *Petrology* **19**, 134–166.

Gordeychik, B., Churikova, T., Kronz, A., Sundermeyer, C., Simakin, A. & Wörner, G. (2018). Growth of, and diffusion in, olivine in ultra-fast ascending basalt magmas from Shiveluch volcano. *Scientific Reports* **8**, 1–15.

Hart, S. R. & Davis, K. E. (1978). Nickel partitioning between olivine and silicate melt. *Earth and Planetary Science Letters* **40**, 203–219.

Holzapfel, C., Chakraborty, S., Rubie, D. C. & Frost, D. J. (2007). Effect of pressure on Fe–Mg, Ni and Mn diffusion in $(Fe_xMg_{1-x})_2SiO_4$ olivine. *Physics of the Earth and Planetary Interiors* **162**, 186–198.

Kahl, M., Chakraborty, S., Costa, F. & Pompilio, M. (2011). Dynamic plumbing system beneath volcanoes revealed by kinetic modeling, and the connection to monitoring data: an example from Mt. Etna. *Earth and Planetary Science Letters* **308**, 11–22.

Kahl, M., Chakraborty, S., Pompilio, M. & Costa, F. (2015). Constraints on the nature and evolution of the magma plumbing system of Mt. Etna volcano (1991–2008) from a combined thermodynamic and kinetic modelling of the compositional record of minerals. *Journal of Petrology* **56**, 2025–2068.

Kamenetsky, V. S., Kamenetsky, M. B., Sobolev, A. V., Golovin, A. V., Demouchy, S., Faure, K., Sharygin, V. V. & Kuzmin, D. V. (2008). Olivine in the Udachnaya-East kimberlite (Yakutia, Russia): types, compositions and origins. *Journal of Petrology* **49**, 823–839.

Kamenetsky, V. S., Kamenetsky, M. B. & Maas, R. (2011). New identity of the kimberlite melt: constraints from unaltered diamondiferous Udachnaya-East Pipe Kimberlite, Russia. In: Chen, D. (ed.) *Advances in Data, Methods, Models and Their Applications in Geoscience*. Rijeka, Croatia: InTech, pp. 181–214.

Kargin, A. V., Sazonova, L. V., Nosova, A. A., Pervov, V. A., Minevrina, E. V., Khvostikov, V. A. & Burmii, Z. P. (2017). Sheared peridotite xenolith from the V. Grib kimberlite pipe, Arkhangelsk Diamond Province, Russia: Texture, composition, and origin. *Geoscience Frontiers* **8**, 653–669.

Kline, S. J. (1986). *Similitude and Approximation Theory*. Berlin: Springer.

Klöck, W. & Palme, H. (1988). Partitioning of siderophile and chalcophile elements between sulfide, olivine, and glass in a naturally reduced basalt from Disko Island, Greenland. In: Ryder, G. (ed.) *Lunar and Planetary Science Conference, 18th, Houston, TX, March 16–20, 1987*. Cambridge: Cambridge University Press; Houston, TX: Lunar and Planetary Institute, pp. 471–483.

Lim, E., Giuliani, A., Phillips, D. & Goemann, K. (2018). Origin of complex zoning in olivine from diverse, diamondiferous kimberlites and tectonic settings: Ekati (Canada), Alto Paranaiba (Brazil) and Kaalvallei (South Africa). *Mineralogy and Petrology* **112**, 539–554.

Lynn, K. J., Garcia, M. O., Shea, T., Costa, F. & Swanson, D. A. (2017a). Timescales of mixing and storage for Keanakāko'i Tephra magmas (1500–1820 C.E.), Kīlauea Volcano, Hawai'i. *Contributions to Mineralogy and Petrology* **172**, article number 76.

Lynn, K. J., Shea, T. & Garcia, M. O. (2017b). Nickel variability in Hawaiian olivine: Evaluating the relative contributions from mantle and crustal processes. *American Mineralogist* **102**, 507–518.

Lynn, K. J., Shea, T., Garcia, M. O., Costa, F. & Norman, M. D. (2018). Lithium diffusion in olivine records magmatic priming of explosive basaltic eruptions. *Earth and Planetary Science Letters* **500**, 127–135.

Matzen, A. K., Wood, B. J., Baker, M. B. & Stolper, E. M. (2017). The roles of pyroxenite and peridotite in the mantle sources of oceanic basalts. *Nature Geoscience* **10**, 530–535.

Mironov, N. L. & Portnyagin, M. V. (2011). H_2O and CO_2 in parental magmas of Kliuchevskoi volcano inferred from study of melt and fluid inclusions in olivine. *Russian Geology and Geophysics* **52**, 1353–1367.

Mironov, N., Portnyagin, M., Botcharnikov, R., Gurenko, A., Hoernle, K. & Holtz, F. (2015). Quantification of the CO_2 budget and H_2O–CO_2 systematics in subduction-zone magmas through the experimental hydration of melt inclusions in olivine at high H_2O pressure. *Earth and Planetary Science Letters* **425**, 1–11.

Mitchell, R. H. (1973). Composition of olivine, silica activity and oxygen fugacity in kimberlite. *Lithos* **6**, 65–81.

Mitchell, R. H. (1986). *Kimberlites. Mineralogy, Geochemistry, and Petrology*. Berlin: Springer.

Mitchell, R. H., Giuliani, A. & O'Brien, H. (2019). What is a kimberlite? Petrology and mineralogy of hypabyssal kimberlites. *Elements* **15**, 381–386.

Moore, A. E (2017). Quantitative modelling of the apparent decoupling of Mg# and Ni in kimberlitic olivine margins: comment on Cordier *et al*. *Journal of Petrology* **58**, 391–390.

Mourey, A. J. & Shea, T. (2019). Forming olivine phenocrysts in basalt: a 3D characterization of growth rates in laboratory experiments. *Frontiers in Earth Science* **7**, 1–16.

Nekrylov, N., Portnyagin, M. V., Kamenetsky, V. S., Mironov, N. L., Churikova, T. G., Plechov, P. Y., Abersteiner, A., Gorbach, N. V., Gordeychik, B. N., Krasheninnikov, S. P., Tobelko, D. P., Shur, M. Y., Tetroeva, S. A., Volynets, A. O., Hoernle, K. & Wörner, G. (2018). Chromium spinel in Late Quaternary

volcanic rocks from Kamchatka: Implications for spatial compositional variability of subarc mantle and its oxidation state. *Lithos* **322**, 212–224.

Newton, I. (1701). Scala graduum caloris. Calorum descriptiones & signa. *Philosophical Transactions of the Royal Society of London* **22**, 824–829.

Nishizawa, T., Nakamura, H., Churikova, T., Gordeychik, B., Ishizuka, O., Haraguchi, S., Miyazaki, T., Vaglarov, B. S., Chang, Q., Hamada, M., Kimura, J.-I., Ueki, K., Toyama, C., Nakao, A. & Iwamori, H. (2017). Genesis of ultra-high-Ni olivine in high-Mg andesite lava triggered by seamount subduction. *Scientific Reports* **7**, 1–11.

Oeser, M., Ruprecht, P. & Weyer, S. (2018). Combined Fe–Mg chemical and isotopic zoning in olivine constraining magma mixing-to-eruption timescales for the continental arc volcano Irazú (Costa Rica) and Cr diffusion in olivine. *American Mineralogist* **103**, 582–599.

Ozerov, A. Y. (2000). The evolution of high-alumina basalts of the Klyuchevskoy volcano, Kamchatka, Russia, based on microprobe analyses of mineral inclusions. *Journal of Volcanology and Geothermal Research* **95**, 65–79.

Petry, C., Chakraborty, S. & Palme, H. (2004). Experimental determination of Ni diffusion coefficients in olivine and their dependence on temperature, composition, oxygen fugacity, and crystallographic orientation. *Geochimica et Cosmochimica Acta* **68**, 4179–4188.

Portnyagin, M. V., Plechov, P. Y., Matveev, S. V., Osipenko, A. B. & Mironov, N. L. (2005). Petrology of avachites, high-magnesian basalts of Avachinsky volcano, Kamchatka: I. General characteristics and composition of rocks and minerals. *Petrology* **13**, 99–121.

Prelević, D., Jacob, D. E. & Foley, S. F. (2013). Recycling plus: a new recipe for the formation of Alpine–Himalayan orogenic mantle lithosphere. *Earth and Planetary Science Letters* **362**, 187–197.

Qian, Q., O'Neill, H. S. C. & Hermann, J. (2010). Comparative diffusion coefficients of major and trace elements in olivine at ~950 °C from a xenocryst included in dioritic magma. *Geology* **38**, 331–334.

Ruprecht, P. & Plank, T. (2013). Feeding andesitic eruptions with a high-speed connection from the mantle. *Nature* **500**, 68–72.

Ruth, D. C. S., Costa, F., Bouvet de Maisonneuve, C., Franco, L., Cortés, J. A. & Calder, E. S. (2018). Crystal and melt inclusion timescales reveal the evolution of magma migration before eruption. *Nature Communications* **9**, 1–9.

Sazonova, L. V., Nosova, A. A., Kargin, A. V., Borisovskiy, S. E., Tretyachenko, V. V., Abazova, Z. M. & Griban', Y. G. (2015). Olivine from the Pionerskaya and V. Grib kimberlite pipes, Arkhangelsk diamond province, Russia: Types, composition, and origin. *Petrology* **23**, 227–258.

Shea, T., Costa, F., Krimer, D. & Hammer, J. E. (2015a). Accuracy of timescales retrieved from diffusion modeling in olivine: A 3D perspective. *American Mineralogist* **100**, 2026–2042.

Shea, T., Lynn, K. J. & Garcia, M. O. (2015b). Cracking the olivine zoning code: Distinguishing between crystal growth and diffusion. *Geology* **43**, 935–938.

Skinner, E. M. W. (1986). Contrasting Group 1 and Group 2 kimberlite petrology: towards a genetic model for kimberlites. In: Smith, C. B. (ed.) *Fourth International Kimberlite Conference. Extended Abstracts. Perth, Western Australia, August 11th–15th, 1986*. Sydney: Geological Society of Australia, pp. 202–204.

Skinner, E. M. W. & Clement, C. R. (1979). Mineralogical classification of Southern African Kimberlites. In: Meyer, H. O. A., and Boyd, F. R. (eds) *Kimberlites, Diatremes, and Diamonds: Their Geology, Petrology, and Geochemistry*. Washington, DC: American Geophysical Union, pp. 129–139.

Straub, S. M., La Gatta, A. B., Pozzo, A. L. M. D. & Langmuir, C. H. (2008). Evidence from high-Ni olivines for a hybridized peridotite/pyroxenite source for orogenic andesites from the central Mexican Volcanic Belt. *Geochemistry, Geophysics, Geosystems* **9** , 1–33.

Straub, S. M., Gomez-Tuena, A., Stuart, F. M., Zellmer, G. F., Espinasa-Perena, R., Cai, Y. & Iizuka, Y. (2011). Formation of hybrid arc andesites beneath thick continental crust. *Earth and Planetary Science Letters* **303**, 337–347.

Sundermeyer, C., Di Muro, A., Gordeychik, B. & Wörner, G. (2020). Timescales of magmatic processes during the eruptive cycle 2014–2015 at Piton de la Fournaise, La Réunion, obtained from Mg–Fe diffusion modelling in olivine. *Contributions to Mineralogy and Petrology* **175**, 1–16.

Thomson, A. & Maclennan, J. (2013). The distribution of olivine compositions in Icelandic basalts and picrites. *Journal of Petrology* **54**, 745–768.

Volynets, O. N., Ponomareva, V. V. & Babansky, A. D. (1997). Magnesian basalts of Shiveluch andesite volcano, Kamchatka. *Petrology* **5**, 183–196.

Wang, Z. & Gaetani, G. A. (2008). Partitioning of Ni between olivine and siliceous eclogite partial melt: experimental constraints on the mantle source of Hawaiian basalts. *Contributions to Mineralogy and Petrology* **156**, 661–678.

Welsch, B., Faure, F., Famin, V., Baronnet, A. & Bachèlery, P. (2013). Dendritic crystallization: a single process for all the textures of olivine in basalts? *Journal of Petrology* **54**, 539–574.